

Lehrstuhl für Informatik 10 (Systemsimulation)



**Fluid flow simulations using the lattice Boltzmann method with multiple
relaxation times**

Christoph Rettinger

Bachelor Thesis

Fluid flow simulations using the lattice Boltzmann method with multiple relaxation times

Christoph Rettinger

Bachelor Thesis

Aufgabensteller:	Prof. Dr. Ulrich Rude
Betreuer:	Dipl.-Ing.(FH) Dominik Bartuschat, M. Sc. (hons) Dipl.-Inf. Simon Bogner
Bearbeitungszeitraum:	29.04.2013 - 06.09.2013

Erklärung:

Ich versichere, dass ich die Arbeit ohne fremde Hilfe und ohne Benutzung anderer als der angegebenen Quellen angefertigt habe und dass die Arbeit in gleicher oder ähnlicher Form noch keiner anderen Prüfungsbehörde vorgelegen hat und von dieser als Teil einer Prüfungsleistung angenommen wurde. Alle Ausführungen, die wörtlich oder sinngemäß übernommen wurden, sind als solche gekennzeichnet.

Der Universität Erlangen-Nürnberg, vertreten durch den Lehrstuhl für Systemsimulation (Informatik 10), wird für Zwecke der Forschung und Lehre ein einfaches, kostenloses, zeitlich und örtlich unbeschränktes Nutzungsrecht an den Arbeitsergebnissen der Bachelor Thesis einschließlich etwaiger Schutzrechte und Urheberrechte eingeräumt.

Erlangen, den 6. September 2013

.....

Abstract

In this thesis, the multiple-relaxation-time model of the collision operator in the lattice Boltzmann method is presented. In contrast to the simple Bhatnagar-Gross-Krook approximation, not only a single but various relaxation parameters are available and can be used to optimise the simulation results. The main idea behind this approach is the construction of a space based on the moments of the particle distribution functions and the usage of a collision matrix. The consequently increased flexibility allows independent control over certain physical properties, like the kinematic and bulk viscosity of the fluid and the placement of the walls represented by no-slip boundary conditions. To compare different collision models and to obtain more insight into the effect of the various relaxation parameters, simulations featuring a Poiseuille flow, a lid-driven cavity flow and a flow past a square cylinder are carried out. The results allow to identify those relaxation parameters that influence certain flow properties the most. Finally, some guidelines are formulated on how to choose the parameters to achieve accurate and stable outcomes.

Contents

1	Introduction	1
2	The lattice Boltzmann method	2
2.1	General theory	2
2.2	The BGK model	5
2.3	The MRT model	6
2.4	The TRT model	12
3	Simulations of different flows	13
3.1	Poiseuille channel flow	13
3.2	Lid-driven square cavity flow	17
3.3	Flow past a square cylinder	27
4	Summary	32
	Bibliography	33

1 Introduction

In many engineering fields, computer simulations have become a very important and useful tool in order to obtain reasonable results for various applications. Since experiments are in general expensive and time-consuming and measurements are difficult to carry out, simulations offer a flexible alternative. This is especially true for the area of fluid dynamics where the use of numerical methods to simulate different flows is inevitable and summed up under the term *computational fluid dynamics* (CFD). For this purpose, different techniques are available, like finite elements or finite volumes. They rely on discretising the governing equations of the flow, namely the Navier-Stokes equations.

The lattice Boltzmann method (LBM) represents a promising and relatively new alternative to the above mentioned techniques. Developed out of the lattice-gas automaton in the 1990s [11], it has successfully been applied to different complex problems in CFD, like multiphase flows and thermal fluids. This method can be regarded as a discretisation of the Boltzmann equation which features a complicated collision operator. Depending on the model to approximate this collision term, one can distinguish different versions of the LBM. The simplest and therefore most often used model is based on the Bhatnagar-Gross-Krook (BGK) approach [1] resulting in a single-relaxation-time (SRT) model. Here, all variables are relaxed linearly in the velocity space towards their equilibrium value with the same factor. It is possible to generalise the idea of linearising the collision operator which results in the multiple-relaxation-time (MRT) model. This allows defining individual relaxation parameters for all the variables by the construction of a collision matrix, providing the maximal number of degrees of freedom to optimise the LBM. Even though it is known to be superior over the SRT model in terms of numerical stability and exact boundary placement, the MRT model is only rarely used because it is said to be too complicated to apply in general.

The aim of this thesis is to present the MRT model in detail and to execute different flow simulations in order to bring attention to the MRT approach and to provide a better insight into its capabilities. For this reason, the LBM together with the BGK model are shortly introduced at first to provide a general understanding of the matter. This is followed by the design of a MRT model as proposed by D. d'Humières [3] in 1992 at first and presented by P. Lallemand and L.-S. Luo [8]. There, a new space, representing the moments, is constructed to relate the relaxation times to physical properties, like the kinematic and the bulk viscosity of the fluid. Due to the necessary transformations between the two spaces, the whole procedure yields a slightly more computationally expensive algorithm than the SRT counterpart. As a compromise regarding complexity and numerical stability, the collision model using two relaxation times (TRT) from I. Ginzburg et al. [6] is briefly shown afterwards. In Sec. 3, three distinct simulation setups are utilised to compare the performance of SRT, TRT and MRT models and to find out more about the effect of different relaxation parameters on flow properties. These tests feature a Poiseuille channel flow similar to C. Pan et al. [10], a lid-driven square cavity flow inspired by L.-S. Luo et al. [9] and J.-S. Wu et al. [12], and at last a flow past a square cylinder according to T. Zeiser [13]. The results suggest that besides the already found relations, two additional relaxation parameters are especially important and need to be taken care of. This allows to finally give some guideline on how to choose the MRT parameters to make benefit out of the degrees of freedom.

2 The lattice Boltzmann method

2.1 General theory

In computational fluid dynamics, one is interested in simulating different fluid flows in various geometries to obtain information about the flow properties in certain regions of the domain. The behaviour of the fluid can be described by the Navier-Stokes equations which consist of the vectorial momentum equation and the scalar continuity equation. For the case of an incompressible fluid, they are given as:

$$\frac{\partial \vec{u}}{\partial t} + (\vec{u} \cdot \nabla) \vec{u} = -\frac{1}{\rho} \nabla p + \nu \Delta \vec{u} \quad (2.1)$$

$$\nabla \cdot \vec{u} = 0 \quad (2.2)$$

For a given density ρ and a kinematic viscosity ν , these equations model the behaviour of velocity \vec{u} and pressure p in time and space. Many numerical methods discretise these equations directly using e.g. finite differences or finite volume techniques to finally arrive at a system of equations that can be solved numerically.

In the 1960s, the so-called lattice-gas cellular automaton (LGCA) from Frisch, Hasslacher and Pomeau was proven to satisfy the Navier-Stokes equations. Here, the space is discretised in cells which are arranged on a regular lattice. Fictive particles, which are used to model the fluid, reside in these cells and can only move in certain discrete directions. Each discrete time step is then split into two parts. At first, the particles move according to their velocity to the neighbouring cells. Afterwards, certain mass and momentum conserving collision rules are applied inside the cell, updating the velocities of the colliding particles. For more information about the LGCA and their development, the book by Wolf-Gladrow [11] serves as a good reference.

Out of the LGCA the lattice Boltzmann method (LBM) was derived a few years later, improving some inherent drawbacks of the LGCA and making it more flexible in its application. This is achieved by replacing the Boolean description of the particles used in the LGCA by continuous particle distribution functions (PDFs).

As the name already suggests, the LBM is related to the Boltzmann equation such that it can be regarded as its discretisation. More information can again be found in [11]. The lattice Boltzmann equation, which describes the evolution of the whole system, is finally given as¹:

$$f_q(\vec{x}_j + \vec{c}_q \delta t, t + \delta t) - f_q(\vec{x}_j, t) = \Omega_q(\vec{x}_j, t), \quad q = 0, \dots, (Q-1), \quad (2.3)$$

where f_q is the q -th component of the vector containing the particle distribution functions, \vec{x}_j is the location of the j -th lattice cell, \vec{c}_q the q -th discrete velocity, δt the time step length and Ω_q the q -th component of the collision operator. Q is the number of discrete velocities and is defined by the choice of the model for the velocity space. In practice, the d2q9 and the d3q19 models are often used for 2D and 3D simulations, respectively. A sketch can be found in Fig. 2.1. In general, such schemes are described with the dDqQ notation, where D is the number of dimensions and Q again the number of the discrete velocities.

Consequently, the d2q9 model features nine discrete velocities. One zero rest velocity in the centre, four velocities pointing towards the neighbouring cells in horizontal and vertical direction and another four velocities towards the diagonal neighbours. These velocities are therefore given as:

¹The notation used throughout this thesis is mostly taken from the current draft of the dissertation of D. Bartuschat.

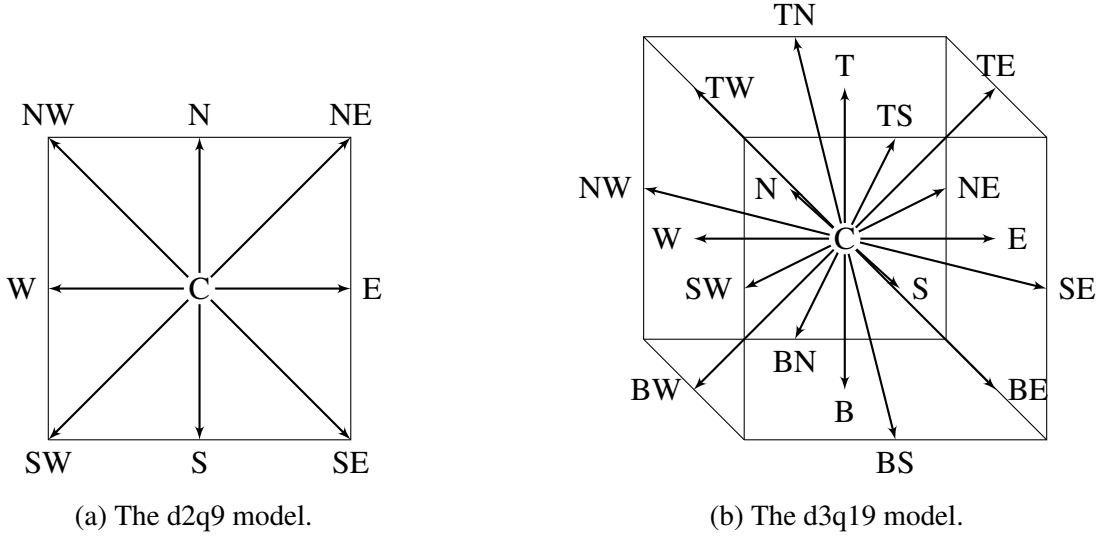


Figure 2.1: The discrete velocities for two popular models.

$$\vec{c}_q = \begin{cases} (0, 0), & q \in \{C\} \\ (\pm c, 0), (0, \pm c), & q \in \{E, N, W, S\} \\ (\pm c, \pm c), & q \in \{NE, NW, SW, SE\} \end{cases} \quad (2.4)$$

where $c = \delta x / \delta t$ is the lattice velocity, defined as the fraction of the lattice spacing δx , i.e. the length of a cell, and the time step length δt . Usually, and also throughout this thesis, one chooses $\delta x = 1$ and $\delta t = 1$ and states all physical values in lattice units. Introducing these nine velocities implies that particles can either stay in the cell or move to the direct neighbours of the current cell. The d2q9 model will be used in the theory part since the resulting equations and formulas are easier to read and understand.

The actual simulations carried out later on are in 3D which makes it necessary to use the d3q19 model. There again, the particle movement is restricted to either resting inside the centre cell or moving to the direct neighbour cells. But from the possible 26 neighbour cells, the ones solely connected to the corners of the central cell are omitted, resulting finally in 19 discrete velocities:

$$\vec{c}_q = \begin{cases} (0, 0, 0), & q \in \{C\} \\ (\pm c, 0, 0), (0, \pm c, 0), (0, 0, \pm c), & q \in \{E, W, N, S, T, B\} \\ (\pm c, \pm c, 0), (0, \pm c, \pm c), (\pm c, 0, \pm c), & q \in \{NE, NW, SE, SW, TE, TW, \\ & BE, BW, TN, TS, BN, BS\} \end{cases} \quad (2.5)$$

Having picked a velocity model, the actual simulation consists of solving Eq. (2.3) in each time step to update the particle distribution functions f_q in each cell. Like in the case of LGCAs, this is achieved by splitting this task into two steps. For that purpose, Eq. (2.3) is reformulated as

$$f_q(\vec{x}_j + \vec{c}_q \delta t, t + \delta t) = f_q(\vec{x}_j, t) + \Omega_q(\vec{x}_j, t) \quad (2.6)$$

making the two steps clearer:

1. collision step

In this step the collision is carried out, i.e. Ω_q is evaluated and used to update f_q . This yields

an updated right hand side of Eq. (2.6).

$$f_q^*(\vec{x}_j, t) = f_q(\vec{x}_j, t) + \Omega_q(\vec{x}_j, t), \quad (2.7)$$

where f_q^* denotes the post-collision value of f_q . The collision is a strictly local operation which takes place in each cell individually. The main task is finding a good model for the collision function Ω_q since the actual formula is unknown. For this purpose, different approximations exist, like the BGK, TRT and MRT models. These three are presented in the following sections in more detail since they form the core part of the LBM algorithm and have a huge effect on the behaviour of the LBM.

2. streaming step

During this step the post-collision value of f_q , i.e. f_q^* , is streamed according to its discrete velocity \vec{c}_q to the next cell:

$$f_q(\vec{x}_j + \vec{c}_q \delta t, t + \delta t) = f_q^*(\vec{x}_j, t) \quad (2.8)$$

In the actual implementation, one distinguishes whether the values are pushed to the neighbour cells or pulled from them. In the first case, each cell explicitly copies their particle distribution functions to the neighbour cells and in the latter one, the cells access the corresponding values of the neighbour cells implicitly during the collision step.

Both steps are local since they require either computations inside the cell or information exchange with the direct neighbour cells. This makes the lattice Boltzmann method especially well suited for supercomputers where the simulation domain is usually decomposed into smaller sub regions which are then distributed across the nodes of the supercomputer. Therefore, only local operations are desired since they omit the need for global communication of all nodes which is in general comparably slow.

In CFD applications, one is usually interested in the values of the fluid velocity and its pressure across the domain. In the LBM setting, these can be directly obtained from the particle distribution functions:

- The density ρ of the fluid inside a cell is defined by the zeroth-order moment of the PDFs which is simply the sum over all PDFs:

$$\rho(\vec{x}_j) = \sum_q f_q(\vec{x}_j) \quad (2.9)$$

- The momentum is the first-order moment and therefore defined as:

$$\rho(\vec{x}_j) \vec{u}(\vec{x}_j) = \sum_q f_q(\vec{x}_j) \vec{c}_q \quad (2.10)$$

In the case of incompressible fluids, the density is assumed to be at a constant reference density ρ_0 which is most often set to 1. Then this equation simplifies to:

$$\vec{u}(\vec{x}_j) = \sum_q f_q(\vec{x}_j) \vec{c}_q \quad (2.11)$$

- The pressure is linearly linked to the density:

$$p(\vec{x}_j) = c_s^2 \rho(\vec{x}_j), \quad (2.12)$$

where $c_s = \frac{1}{\sqrt{3}}c$ is the lattice speed of sound.

Another important aspect of numerical methods are boundary conditions. As for the LBM, there exist various boundary conditions for different types of boundaries. In the simulations described later on, bounce-back boundary conditions are used to model steady and moving walls (cf. e.g. [9]) and pressure anti-bounce-back boundary conditions are utilised to approximate a Dirichlet boundary condition for the pressure (cf. [6]).

2.2 The BGK model

As mentioned in the previous section, the collision operator Ω_q in Eq. (2.7) needs to be modelled. Bhatnagar, Gross and Krook suggested to use the following approximation [1]:

$$\Omega_q = -\frac{1}{\tau} (f_q - f_q^{eq}) \quad (2.13)$$

Here, τ is the relaxation time and f_q^{eq} is an approximation of the Maxwellian equilibrium distribution function. τ models the mean time between two particle collisions and is directly linked to the kinematic viscosity of the fluid [8]:

$$\nu = \frac{1}{3} \left(\tau - \frac{1}{2} \right) \quad (2.14)$$

The equilibrium distribution functions f_q^{eq} are given by:

$$f_q^{eq}(\rho, \vec{u}) = \rho w_q \left[1 + \frac{1}{c_s^2} (\vec{c}_q \cdot \vec{u}) + \frac{1}{2c_s^4} (\vec{c}_q \cdot \vec{u})^2 - \frac{1}{2c_s^2} (\vec{u} \cdot \vec{u}) \right], \quad (2.15)$$

where the w_q are weightings for different directions. In the case of the d2q9 model, these are

$$w_q = \begin{cases} 4/9, & q \in \{C\} \\ 1/9, & q \in \{E, N, W, S\} \\ 1/36, & q \in \{NE, NW, SW, SE\} \end{cases} \quad (2.16)$$

and for the d3q19 model

$$w_q = \begin{cases} 1/3, & q \in \{C\} \\ 1/18, & q \in \{E, W, N, S, T, B\} \\ 1/36, & q \in \{NE, NW, SE, SW, TE, TW, \\ & BE, BW, TN, TS, BN, BS\}. \end{cases} \quad (2.17)$$

The idea behind this approximation is that the collision relaxes the particle distributions linearly towards their equilibrium values which are defined by the Maxwell distribution.

This so-called BGK model is the most widely known collision model and is often used because of its simplicity. Since it features only one relaxation time, τ , it will be referred to as single-relaxation-time (SRT) model throughout this thesis.

2.3 The MRT model

The linearised collision operator can also be approximated in a more general fashion. This is achieved by using a collision matrix \mathbf{S} instead of the single relaxation time in the BGK model.

$$\bar{\Omega} = -\mathbf{S} \left(\vec{f} - \vec{f}^{eq} \right) \quad (2.18)$$

The BGK model can immediately be recovered by choosing $\mathbf{S} = \frac{1}{\tau} \mathbf{I}$, where \mathbf{I} denotes the identity matrix.

This general formulation offers the maximum number of degrees of freedom for modelling the linearised collision operator and forms the basis of the multiple-relaxation-time (MRT) model. One can now try to assemble the collision matrix directly as it is done e.g. by Higuera et al. [7]. In this thesis, however, another approach to determine the elements of the matrix is utilised which was first proposed by d’Humières [3] in 1992. Here, an additional space, the moment space \mathbb{M} , is constructed in which the collision is carried out. In the following, the d2q9 model (Fig. 2.1a) is used for the derivation of the different parts of the collision model as presented by Lallemand and Luo [8]. Afterwards, the results for the d3q19 model (Fig. 2.1b) are stated since this model is used for the simulations in Sec. 3.

At first, the notion of the velocity space \mathbb{V} is introduced. This space is spanned by the nine discrete velocities of the d2q9 model and is the space in which the collision of the BGK model is carried out. In addition to this one, the moment space \mathbb{M} is constructed, based upon nine independent moments of the PDFs f_q . These moments can now be physically interpreted as e.g. hydrodynamic quantities and their fluxes. This incorporates the physics into the model, making it easier to relate the different relaxation times to e.g. transport coefficients.

For the d2q9 model, one typically chooses the following moments which span the moment space:

- density (0th order): ρ
- energy (2nd order): e
- energy-square (4th order): ϵ
- momentum in x- and y-direction (1st order): j_x and j_y
- heat flow in x- and y-direction (3rd order): q_x and q_y
- diagonal and off-diagonal stress (2nd order): p_{xx} and p_{xy}

The order of the moment is given in brackets. These moments can now be computed out of the PDFs with the help of corresponding moment vectors. These are given by the following formulas:

$$\vec{\rho}_q = |\vec{c}_q|^0 = 1 \quad (2.19)$$

$$\vec{e}_q = -4|\vec{c}_q|^0 + 3 \left((\vec{c}_q)_x^2 + (\vec{c}_q)_y^2 \right) \quad (2.20)$$

$$\vec{\epsilon}_q = 4|\vec{c}_q|^0 - \frac{21}{2} \left((\vec{c}_q)_x^2 + (\vec{c}_q)_y^2 \right) + \frac{9}{2} \left((\vec{c}_q)_x^2 + (\vec{c}_q)_y^2 \right)^2 \quad (2.21)$$

$$\vec{j}_{x,q} = (\vec{c}_q)_x \quad (2.22)$$

$$\vec{q}_{x,q} = \left[-5|\vec{c}_q|^0 + 3 \left((\vec{c}_q)_x^2 + (\vec{c}_q)_y^2 \right) \right] (\vec{c}_q)_x^2 \quad (2.23)$$

$$\vec{j}_{y,q} = (\vec{c}_q)_y \quad (2.24)$$

$$\vec{q}_{y,q} = \left[-5|\vec{c}_q|^0 + 3 \left((\vec{c}_q)_x^2 + (\vec{c}_q)_y^2 \right) \right] (\vec{c}_q)_y^2 \quad (2.25)$$

$$\vec{p}_{xx,q} = (\vec{c}_q)_x^2 - (\vec{c}_q)_y^2 \quad (2.26)$$

$$\vec{p}_{xy,q} = (\vec{c}_q)_x (\vec{c}_q)_y \quad (2.27)$$

The actual moments can then be obtained by the inner product of the PDF vector and the respective moment vector. E.g. the density $\rho = \langle \vec{\rho}, \vec{f} \rangle = \langle \vec{f}, \vec{\rho} \rangle$ which is just a different way of writing Eq. (2.9). The same can be done for the other eight moments.

If one now defines a vector that consists of all the nine moments

$$\vec{m} = (\rho, e, \epsilon, j_x, q_x, j_y, q_y, p_{xx}, p_{xy})^\top, \quad (2.28)$$

the relation between the PDFs and \vec{m} can be expressed with the help of a transformation matrix \mathbf{M} :

$$\vec{m} = \mathbf{M} \vec{f} \quad (2.29)$$

$$\vec{f} = \mathbf{M}^{-1} \vec{m} \quad (2.30)$$

This transformation matrix is given as

$$\mathbf{M} = \begin{pmatrix} \vec{\rho}^\top \\ \vec{e}^\top \\ \vec{\epsilon}^\top \\ \vec{j}_x^\top \\ \vec{q}_x^\top \\ \vec{j}_y^\top \\ \vec{q}_y^\top \\ \vec{p}_{xx}^\top \\ \vec{p}_{xy}^\top \end{pmatrix} = \begin{pmatrix} 1 & 1 & 1 & 1 & 1 & 1 & 1 & 1 & 1 \\ -4 & -1 & -1 & -1 & -1 & 2 & 2 & 2 & 2 \\ 4 & 2 & 2 & 2 & 2 & 1 & 1 & 1 & 1 \\ 0 & 1 & 0 & -1 & 0 & 1 & -1 & -1 & 1 \\ 0 & -2 & 0 & 2 & 0 & 1 & -1 & -1 & 1 \\ 0 & 0 & 1 & 0 & -1 & 1 & 1 & -1 & -1 \\ 0 & 0 & -2 & 0 & 2 & 1 & 1 & -1 & -1 \\ 0 & 1 & -1 & 1 & -1 & 0 & 0 & 0 & 0 \\ 0 & 0 & 0 & 0 & 0 & 1 & -1 & 1 & -1 \end{pmatrix} \quad (2.31)$$

and transforms a vector of the velocity space \mathbb{V} into a vector of the moment space \mathbb{M} . The ordering of its rows is not arbitrary but represents the order of the tensors of the moments: ρ, e and ϵ are scalars and therefore zeroth-order tensors. j_x, q_x, j_y and q_y are components of vectors, i.e. first-order tensors, and p_{xx} and p_{xy} are components of second-order tensors.

With the help of this transformation matrix, Eq. (2.18) can be rewritten as

$$\vec{\Omega} = -\mathbf{M}^{-1} \hat{\mathbf{S}} (\vec{m} - \vec{m}^{eq}), \quad (2.32)$$

where the former collision matrix has been replaced by $\mathbf{S} = \mathbf{M}^{-1} \hat{\mathbf{S}} \mathbf{M}$. The new collision matrix $\hat{\mathbf{S}}$ is a diagonal matrix

$$\hat{\mathbf{S}} = \text{diag}(s_0, \dots, s_8) \quad (2.33)$$

which has nine relaxation parameters s_q on its diagonal. For stability reasons, each s_q must lie between 0 and 2. Therefore, the previous task of specifying the 9×9 elements of \mathbf{S} has been reduced to find formulas for these nine relaxation parameters.

To relate these s_q to the moments, one now has a look at the relaxation equations of the different moments. They are given as:

$$\rho^* = \rho - s_0 [\rho - \rho^{eq}] \quad (2.34)$$

$$e^* = e - s_1 [e - e^{eq}] \quad (2.35)$$

$$\epsilon^* = \epsilon - s_2 [\epsilon - \epsilon^{eq}] \quad (2.36)$$

$$j_x^* = j_x - s_3 [j_x - j_x^{eq}] \quad (2.37)$$

$$q_x^* = q_x - s_4 [q_x - q_x^{eq}] \quad (2.38)$$

$$j_y^* = j_y - s_5 [j_y - j_y^{eq}] \quad (2.39)$$

$$q_y^* = q_y - s_6 [q_y - q_y^{eq}] \quad (2.40)$$

$$p_{xx}^* = p_{xx} - s_7 [p_{xx} - p_{xx}^{eq}] \quad (2.41)$$

$$p_{xy}^* = p_{xy} - s_8 [p_{xy} - p_{xy}^{eq}], \quad (2.42)$$

where $*$ denotes the post-collision value. These equations again represent the assumption that the moments, like the PDFs in the BGK model, relax linearly towards their equilibrium values which come from the Maxwellian molecules theory.

The density ρ and the components of the momentum, j_x and j_y , are the conserved quantities of the system and are called *hydrodynamic* moments. They therefore are equal to their equilibrium values. Consequently, the relaxation parameters s_0 , s_3 and s_5 have no influence and are by convention set to zero.

$$s_0 = s_3 = s_5 = 0 \quad (2.43)$$

The other moments are the non-conserved, *kinetic* ones, which are affected by collisions. In order to evaluate the relaxation equations of those moments, their equilibrium functions e^{eq} , ϵ^{eq} , q_x^{eq} , q_y^{eq} , p_{xx}^{eq} and p_{xy}^{eq} are needed. Generally, they can be chosen at will but with respect to the symmetry of the problem. Luo et al. [9] state the following formulas which only depend on the hydrodynamic moments:

$$e^{eq} = -2\rho + 3(j_x^2 + j_y^2) \quad (2.44)$$

$$\epsilon^{eq} = \rho - 3(j_x^2 + j_y^2) \quad (2.45)$$

$$q_x^{eq} = -j_x \quad (2.46)$$

$$q_y^{eq} = -j_y \quad (2.47)$$

$$p_{xx}^{eq} = j_x^2 - j_y^2 \quad (2.48)$$

$$p_{xy}^{eq} = j_x j_y \quad (2.49)$$

To get formulas that relate physical quantities, like viscosity, to the relaxation rates of the kinetic moments, one can apply a Chapman-Enskog-Expansion. Another approach is a linearisation of the lattice Boltzmann equation, cf. [8]. Here, the collision operator is linearised, then transferred to the Fourier space where one obtains a wave vector \vec{k} . Then an eigenvalue problem is constructed to see the effect of different \vec{k} s on e.g. physical quantities and stability. This results in the following

relations:

$$s_1 = \frac{2}{6\zeta + 1} \quad (2.50)$$

$$s_4 = s_6 \quad (2.51)$$

$$s_7 = s_8 = \frac{2}{6\nu + 1}, \quad (2.52)$$

where ζ is the bulk or volume viscosity, which is responsible for damping density and pressure fluctuations. For s_2, s_4 and s_6 no formulas can be found by the stability analysis. Since s_2 corresponds to a similar but higher order moment as s_1 (energy and energy-square), s_2 is said to have some small influence on the bulk viscosity as well. In case of a Poiseuille flow, Luo et al. state the following formula which relates s_4 and the simulated boundary position [9]:

$$\Delta = \frac{4}{3} \left(\frac{1}{s_8} - \frac{1}{2} \right) \left(\frac{1}{s_4} - \frac{1}{2} \right), \quad (2.53)$$

where Δ is the distance of the near-wall node to the real wall. Therefore, only when s_4 , and consequently also s_6 , satisfy this relation and $\Delta = 1/2$, the no-slip boundary conditions at the wall are indeed simulated. Since the value of s_8 is already fixed to obtain a specific kinematic viscosity ν according to Eq. (2.52), s_4 and s_6 are the relaxation rates that are used to place the boundary on the exact position.

Now all necessary parts of the MRT model are obtained and a new LBM algorithm can be formulated:

1. Transform \vec{f} into a vector of the moment space \mathbb{M} by

$$\vec{m} = \mathbf{M} \vec{f}, \quad (2.54)$$

where the transformation matrix \mathbf{M} is given by (2.31).

2. Compute the equilibrium values of the moments, \vec{m}^{eq} , according to Eqs. (2.44-2.49).
3. Execute the collision in the moment space

$$\Delta \vec{m} = \hat{\mathbf{S}} [\vec{m} - \vec{m}^{eq}], \quad (2.55)$$

using the diagonal collision matrix $\hat{\mathbf{S}}$ from (2.33).

4. Transform $\Delta \vec{m}$ back into a vector of the velocity space \mathbb{V} , using

$$\Delta \vec{f} = \mathbf{M}^{-1} \Delta \vec{m}. \quad (2.56)$$

5. Perform the streaming step

$$f_q(\vec{x}_j + \vec{c}_q \delta t, t + \delta t) = f_q(\vec{x}_j, t) - \Delta f_q. \quad (2.57)$$

One can see that the main differences between this algorithm and the one for the BGK model are the transformations between the two spaces which were not needed before. These cause a computational overhead that is about 10% - 20% of the performance of the BGK algorithm [4].

Following, the different parts of the MRT model for the d3q19 velocity layout according to [4] are presented since this one is later needed for the simulations. Here, the velocity space \mathbb{V} is now spanned by 19 discrete velocities as sketched in Fig. 2.1b. At first, the moments that specify the moment space \mathbb{M} are chosen. Similar to the d2q9 model, the density ρ , energy e , energy-square ϵ , the x-, y-, z-components of the momentum, j_x, j_y, j_z , and of the heat flux, q_x, q_y, q_z , and some stress tensor components, $3p_{xx}, p_{ww} = p_{yy} - p_{zz}, p_{xy}, p_{yz}, p_{xz}$, are used. The set is completed by three moments of cubic order m_x, m_y, m_z , which are part of a third rank tensor, and two of quartic order, $3\pi_{xx}, \pi_{ww}$. These are collected in the moment vector \vec{m} :

$$\vec{m} = (\rho, e, \epsilon, j_x, q_x, j_y, q_y, j_z, q_z, 3p_{xx}, 3\pi_{xx}, p_{ww}, \pi_{ww}, p_{xy}, p_{yz}, p_{xz}, m_x, m_y, m_z)^\top \quad (2.58)$$

Again, formulas for the corresponding vectors can be evaluated that allow the calculation of these 19 moments out of the PDFs. Those can be found in [4]. With these, the transformation matrix \mathbf{M} can be derived, which is now a 19×19 matrix.

$$\mathbf{M} = \begin{pmatrix} \bar{\rho}^\top \\ \bar{e}^\top \\ \bar{\epsilon}^\top \\ \bar{j}_x^\top \\ \bar{q}_x^\top \\ \bar{j}_y^\top \\ \bar{q}_y^\top \\ \bar{j}_z^\top \\ \bar{q}_z^\top \\ 3\bar{p}_{xx}^\top \\ 3\bar{\pi}_{xx}^\top \\ \bar{p}_{ww}^\top \\ \bar{\pi}_{ww}^\top \\ \bar{p}_{xy}^\top \\ \bar{p}_{yz}^\top \\ \bar{p}_{xz}^\top \\ \bar{m}_x^\top \\ \bar{m}_y^\top \\ \bar{m}_z^\top \end{pmatrix} = \begin{pmatrix} 1 & 1 & 1 & 1 & 1 & 1 & 1 & 1 & 1 & 1 & 1 & 1 & 1 & 1 & 1 & 1 & 1 & 1 & 1 \\ -30 & -11 & -11 & -11 & -11 & -11 & -11 & 8 & 8 & 8 & 8 & 8 & 8 & 8 & 8 & 8 & 8 & 8 & 8 \\ 12 & -4 & -4 & -4 & -4 & -4 & -4 & 1 & 1 & 1 & 1 & 1 & 1 & 1 & 1 & 1 & 1 & 1 & 1 \\ 0 & 1 & -1 & 0 & 0 & 0 & 0 & 1 & -1 & 1 & -1 & 1 & -1 & 1 & -1 & 0 & 0 & 0 & 0 \\ 0 & -4 & 4 & 0 & 0 & 0 & 0 & 1 & -1 & 1 & -1 & 1 & -1 & 1 & -1 & 0 & 0 & 0 & 0 \\ 0 & 0 & 0 & 1 & -1 & 0 & 0 & 1 & 1 & -1 & -1 & 0 & 0 & 0 & 0 & 1 & -1 & 1 & -1 \\ 0 & 0 & 0 & -4 & 4 & 0 & 0 & 1 & 1 & -1 & -1 & 0 & 0 & 0 & 0 & 1 & -1 & 1 & -1 \\ 0 & 0 & 0 & 0 & 0 & 1 & -1 & 0 & 0 & 0 & 0 & 1 & 1 & -1 & -1 & 1 & 1 & -1 & -1 \\ 0 & 0 & 0 & 0 & 0 & -4 & 4 & 0 & 0 & 0 & 0 & 1 & 1 & -1 & -1 & 1 & 1 & -1 & -1 \\ 0 & 2 & 2 & -1 & -1 & -1 & -1 & 1 & 1 & 1 & 1 & 1 & 1 & 1 & 1 & -2 & -2 & -2 & -2 \\ 0 & -4 & -4 & 2 & 2 & 2 & 2 & 1 & 1 & 1 & 1 & 1 & 1 & 1 & 1 & -2 & -2 & -2 & -2 \\ 0 & 0 & 0 & 1 & 1 & -1 & -1 & 1 & 1 & 1 & 1 & -1 & -1 & -1 & -1 & 0 & 0 & 0 & 0 \\ 0 & 0 & 0 & -2 & -2 & 2 & 2 & 1 & 1 & 1 & 1 & -1 & -1 & -1 & -1 & 0 & 0 & 0 & 0 \\ 0 & 0 & 0 & 0 & 0 & 0 & 0 & 1 & -1 & -1 & 1 & 0 & 0 & 0 & 0 & 0 & 0 & 0 & 0 \\ 0 & 0 & 0 & 0 & 0 & 0 & 0 & 0 & 0 & 0 & 0 & 0 & 0 & 0 & 0 & 1 & -1 & -1 & 1 \\ 0 & 0 & 0 & 0 & 0 & 0 & 0 & 0 & 0 & 0 & 0 & 1 & -1 & -1 & 1 & 0 & 0 & 0 & 0 \\ 0 & 0 & 0 & 0 & 0 & 0 & 0 & 1 & -1 & 1 & -1 & -1 & 1 & -1 & 1 & 0 & 0 & 0 & 0 \\ 0 & 0 & 0 & 0 & 0 & 0 & 0 & -1 & -1 & 1 & 1 & 0 & 0 & 0 & 0 & 1 & -1 & 1 & -1 \\ 0 & 0 & 0 & 0 & 0 & 0 & 0 & 0 & 0 & 0 & 0 & 1 & 1 & -1 & -1 & -1 & -1 & 1 & 1 \end{pmatrix} \quad (2.59)$$

The elements in the fourth, sixth and eighth row, i.e. the ones corresponding to the components of the momentum, uniquely define the ordering of the velocity set.

For the collision in the moment space, the equilibrium values for the kinetic moments are needed and are defined as:

$$e^{eq} = -11\rho + \frac{19}{\rho_0} (j_x^2 + j_y^2 + j_z^2) \quad (2.60) \quad p_{ww}^{eq} = \frac{1}{\rho_0} (j_y^2 - j_z^2) \quad (2.66)$$

$$\epsilon^{eq} = \omega_\epsilon \rho + \frac{\omega_{\epsilon j}}{\rho_0} (j_x^2 + j_y^2 + j_z^2) \quad (2.61) \quad p_{xy}^{eq} = \frac{1}{\rho_0} j_x j_y \quad (2.67)$$

$$q_x^{eq} = -\frac{2}{3} j_x \quad (2.62) \quad p_{yz}^{eq} = \frac{1}{\rho_0} j_y j_z \quad (2.68)$$

$$q_y^{eq} = -\frac{2}{3} j_y \quad (2.63) \quad p_{xz}^{eq} = \frac{1}{\rho_0} j_x j_z \quad (2.69)$$

$$q_z^{eq} = -\frac{2}{3} j_z \quad (2.64) \quad \pi_{xx}^{eq} = \omega_{xx} p_{xx}^{eq} \quad (2.70)$$

$$p_{xx}^{eq} = \frac{1}{3\rho_0} [2j_x^2 - (j_y^2 + j_z^2)] \quad (2.65) \quad \pi_{ww}^{eq} = \omega_{xx} p_{ww}^{eq} \quad (2.71)$$

$$m_x^{eq} = m_y^{eq} = m_z^{eq} = 0 \quad (2.72)$$

In these formulas the approximation $1/\rho \approx 1/\rho_0$ is used, where ρ_0 is the constant mean density in the system which is typically set to be 1. As stated in [4], this helps to reduce compressibility effects. The appearing parameters $\omega_\epsilon, \omega_{\epsilon j}$ and ω_{xx} are additional free parameters.

The diagonal collision matrix $\hat{\mathbf{S}}$ is now given as:

$$\hat{\mathbf{S}} = \text{diag}(0, s_1, s_2, 0, s_4, 0, s_4, 0, s_4, s_9, s_{10}, s_9, s_{10}, s_{13}, s_{13}, s_{13}, s_{16}, s_{16}, s_{16}), \quad (2.73)$$

where it is already used that the relaxation parameters for conserved moments are zero and a few other parameters are equal for some kinetic moments. Two of the relaxation parameters are related to the kinematic viscosity

$$s_9 = s_{13} = \frac{2}{6\nu + 1} \quad (2.74)$$

and s_1 is related to the bulk viscosity over

$$s_1 = \frac{2}{9\zeta + 1}. \quad (2.75)$$

Through linear stability analysis, d'Humières et al. found the following values for s_q and ω to be 'optimal' [4]:

$$s_1 = 1.19, s_2 = s_{10} = 1.4, s_4 = 1.2, s_{16} = 1.98, \quad (2.76)$$

$$\omega_\epsilon = 0, \omega_{\epsilon j} = -\frac{475}{63}, \omega_{xx} = 0. \quad (2.77)$$

This parameter set is the one that is used for the MRT model throughout the simulations in Sec. 3 until otherwise stated. From the findings of the d2q9 model, one can assume that again some of these parameters are linked to the wall placement as given in Eq. (2.53). The Poiseuille flow simulations in Sec. 3.1 suggest that for the d3q19 model these are two parameters, namely s_4 and s_{16} .

As stated in the beginning of this section, the MRT model is a generalisation of the linear collision models and therefore the BGK model can be recovered. For this purpose one has to set all the relaxation parameters $s_q = 1/\tau$ and the free parameters as:

$$\omega_\epsilon = 3, \omega_{\epsilon j} = -\frac{11}{2}, \omega_{xx} = -\frac{1}{2} \quad (2.78)$$

At last, one implementation detail for the MRT model needs to be mentioned explicitly. The necessary transformations from the velocity space to the moment space, Eq. (2.54), and back, Eq. (2.56), are not implemented as matrix-vector multiplications. Instead, they are hard-coded in the programme to make benefit out of the many zero entries in the transformation matrix \mathbf{M} . Also the calculation of the inverse of \mathbf{M} can be circumvented by using the formula given in [4]:

$$\Delta \vec{f} = \mathbf{M}^\top (\mathbf{M} \mathbf{M}^\top)^{-1} \Delta \vec{m} \quad (2.79)$$

This equation uses the fact that $\mathbf{M} \mathbf{M}^\top$ is a diagonal matrix because the rows of \mathbf{M} are the vectors that span the moment space. Those are mutually orthogonal to each other and therefore only the inner product of those vectors with themselves remains on the diagonal. The advantage of this equation is now that a multiplication with the inverse of a diagonal matrix is simply a multiplication with the reciprocal of the diagonal elements of $\mathbf{M} \mathbf{M}^\top$ which again can be done without utilising a real matrix-vector multiplication. The remaining multiplication with \mathbf{M}^\top is also hard-coded to use the zero entries of \mathbf{M} .

2.4 The TRT model

Since it will be used in the simulations in Sec. 3 to compare it with SRT and MRT models, the two-relaxation-time (TRT) model will shortly be presented here. In contrast to the BGK model, it now uses two relaxation times to model the collision operator. The idea is to relax the even-order non-conserved moments with the relaxation rate s_+ and the odd-order ones with s_- . When comparing with the numeration on page 6, it gets clear that for the d2q9 model e, ϵ, p_{xx} and p_{xy} are the even-order moments and q_x and q_y the odd-order ones. For the d3q19 model, q_x, q_y, q_z, m_x, m_y and m_z are the odd-order moments.

s_+ is equal to the single relaxation rate in the BGK model and therefore is used to control the kinematic viscosity:

$$s_+ = \frac{1}{\tau} = \frac{2}{6\nu + 1} \quad (2.80)$$

s_- is chosen just like s_4 in Eq. (2.53) with $\Delta = 1/2$:

$$s_- = 8 \frac{2 - s_+}{8 - s_+} = 8 \frac{2\tau - 1}{8\tau - 1} = \frac{16\nu}{8\nu + 1} \quad (2.81)$$

This choice enables the TRT model, in contrast to the SRT model, to have exact boundary placement in the Poiseuille flow. Since this is one of the main features of the TRT model, s_- will be called s_{TRT} throughout this thesis. More information about the TRT model can be found e.g. in [5] and [6] from Ginzburg et al.

3 Simulations of different flows

In the following sections, different typical flow problems are simulated and the results obtained by the SRT, TRT and MRT models are compared regarding stability and accuracy. Additionally, it is observed how changing different free parameters in the MRT model will effect the outcomes. This will allow to give some guidance on how to choose them. The simulations are carried out inside the waLBerla² (widely applicable Lattice Boltzmann solver from Erlangen) framework which is developed at the Chair for System Simulation at the Friedrich-Alexander-Universität Erlangen-Nürnberg. This framework allows to simulate various flows and to run the programme in parallel. As a part of this thesis, it has been extended by the MRT model for the d3q19 velocity scheme.

3.1 Poiseuille channel flow

A very common test case is the Poiseuille channel flow in which fluid flows through a channel with a given height and infinite length and width. Though very simple, this simulation setup allows to study flow properties near the boundaries which is of great interest. From fluid mechanics, one expects the velocity to be zero at the boundary to fulfil the no-slip condition there. In this special channel flow, even the whole flow profile can easily be checked since there exists an analytical solution for the laminar case.

Setup

In the following tests, the simulated channel has a height of 16 grid cells in z-direction and at the wall no-slip boundary conditions are applied. These are realised by simple bounce-back boundary conditions. To model the infinite width of the channel, periodic boundary conditions are applied in y-direction. It is important to choose the correct boundary condition in x-direction which is the direction of the flow. At first glance, the use of a uniform inflow velocity might seem suitable. But to be able to compare the results with the analytical solution, a fully developed flow profile is needed. This would require that the channel is very long, resulting in unnecessary many grid cells and consequently long runtimes of the programme. Instead, another possibility to generate a flow is used here, namely external forcing. Here, a constant external force $\vec{g} = (g, 0, 0)^\top$ is applied to all cells. This can be interpreted as a gravitational force acting on the fluid. Together with additional periodic boundary conditions in x-direction, this results after some time in a steady flow and therefore a fully developed velocity profile. This profile can now be compared with the analytical solution which is given as [10]:

$$u_x(z) = \frac{g}{2\nu} (h^2 - z^2), \quad |z| \leq h, \quad (3.1)$$

where h is half of the channel height and ν is the kinematic viscosity of the fluid.

To use external forcing, the LBM algorithm has to be extended by the following [6]:

- calculation of the force F :

$$F_q = 3 w_q \rho \langle \vec{c}_q, \vec{g} \rangle, \quad q = 0, \dots, 18, \quad (3.2)$$

where w_q are the weighting factors from Eq. (2.17), ρ is the density, $\langle \vec{c}_q, \vec{g} \rangle$ is the inner product of the discrete velocity \vec{c}_q and the external force vector \vec{g} .

²<http://www10.informatik.uni-erlangen.de/en/Research/Projects/walberla/description.shtml>

- application of the force to the probability distribution functions f_q :

$$f_q \leftarrow f_q + F_q, \quad q = 0, \dots, 18 \quad (3.3)$$

- to obtain the correct velocity, $0.5 \vec{g}$ has to be added to the velocity since Eq. (2.11) is no longer valid in the presence of external forces.

In all test cases, the external force \vec{g} is chosen to be constant $(0.00001, 0, 0)^\top$ and the overall domain size is $[0, 16] \times [0, 16] \times [0, 16]$. To achieve a steady state solution, the simulation is run 100000 time steps.

Methods

With this test case, the SRT, TRT and MRT models can be compared regarding their capability to ensure a zero velocity at the boundaries at different Reynolds numbers. It is well known from literature, cf. e.g. [9], that the SRT model can not fulfil this condition in general and will yield a velocity profile that is shifted by a constant value compared to the analytically calculated profile. This can be interpreted in two ways: Either the channel, that is simulated, features walls that are not steady but move with a constant velocity. Or the simulated channel width is actually smaller or larger than intended. The TRT model, on the other hand, is constructed to satisfy the no-slip condition in the Poiseuille flow exactly. The profile obtained by the TRT model should thus match the analytical one. As mentioned before, the MRT model is a generalisation of the two other models, i.e. the free parameters and relaxation times can be chosen in such a way that either the SRT or the TRT model are recovered. Therefore, these simulations are first of all used as a validation of the implementation since the ‘real’ SRT or TRT model and the MRT model reduced to a SRT or TRT model, respectively, must yield the same results. Afterwards, the effect of the different free MRT parameters is examined, similar to [10]. For that, the parameter setups described in Tab. 3.1 are used.

	s_1	s_2	s_4	s_{10}	s_{16}
SRT	$1/\tau$	$1/\tau$	$1/\tau$	$1/\tau$	$1/\tau$
TRT	$1/\tau$	$1/\tau$	s_{TRT}	$1/\tau$	s_{TRT}
MRT	1.19	1.4	1.2	1.4	1.98
MRT-1	1.98	1.98	s_{TRT}	1.98	s_{TRT}
MRT-2	$1/\tau$	$1/\tau$	s_{TRT}	$1/\tau$	1.98
MRT-3	$1/\tau$	$1/\tau$	1.98	$1/\tau$	s_{TRT}

Table 3.1: Different relaxation parameters for the Poiseuille flow simulation, s_{TRT} is given in Eq. (2.81).

As mentioned on page 10, the d3q19 MRT model also has three additional free parameters, ω_ϵ , $\omega_{\epsilon j}$ and ω_{xx} , which are used in the formula for calculating the equilibrium moments, cf. Eqs. (2.61), (2.70), (2.71). Since Pan et al. use in their paper for these free parameters only the setup that recovers the SRT/TRT model, cf. Eq. (2.78), it is also tested if changing these parameter values to the ones that d’Humières found to be optimal in [4] alters the results. The values for these parameters can be found in Eq. (2.77).

Results

At first, $\tau = 2.0$ is used and the overall results of SRT, TRT and the MRT model, that d’Humières proposed as the most stable one, are compared in Fig. 3.1.

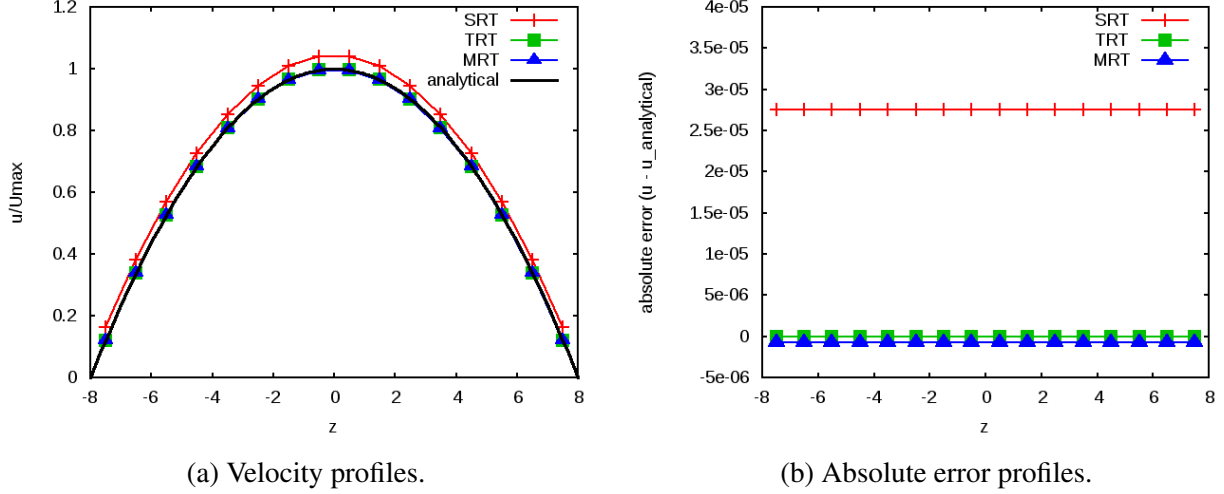


Figure 3.1: Comparison of the velocity profiles, normalised by the analytical maximum velocity, and the absolute error profiles using the SRT, TRT and MRT model and setting $\tau = 2.0$.

Clearly, the shift of the velocity profile can be seen in the SRT model whereas the profiles of the TRT and MRT schemes seem to match the analytical solution quite well. Note that the velocities can not be evaluated directly at the wall ($z = \pm 8$) since the values are stored in the middle of the cells i.e. at $z = -7.5, -6.5 \dots 6.5, 7.5$. The shift can be measured by calculating the absolute error, as plotted in Fig. 3.1b. As expected, the error is constant at each grid point and very large for the SRT model. But also the MRT scheme, in contrast to the TRT model, has introduced a small shift.

When choosing the MRT relaxation parameters in order to recover the SRT and the TRT model as stated in Tab. 3.1, the obtained results are exactly the same as with the real SRT and TRT models. This indicates that the MRT model is correctly implemented.

Another interesting outcome is that apparently it does not matter in this test case if the three free parameters, ω_ϵ , $\omega_{\epsilon j}$ and ω_{xx} , are chosen either to recover the SRT model or to obtain optimal stability. In both cases the results, which are not shown here explicitly, match exactly.

To find out which relaxation rates influence the shift of the profile, the parameter setups from Tab. 3.1 are simulated at different values for τ . The resulting relative errors are measured in the following norm:

$$E(u) = \frac{\sum_z (u(z) - u^*(z))^2}{\sum_z (u^*(z))^2}, \quad (3.4)$$

where u^* is the analytical solution and u the velocity obtained by the simulation. The found values for the error are summarised in Tab. 3.2.

The TRT model, which was especially designed for this purpose, can nearly recover the exact solution. In contrast to that, the SRT model has no additional parameter that can tune the error here, yielding a rather large τ -dependent error which grows for increasing values of τ . The MRT model results also in some quite high errors which are for small τ values close to the SRT errors but decrease slowly for larger τ .

It can be seen that the errors of MRT-1 and TRT are always identical and very close to zero. Both models set the relaxation parameters $s_4 = s_{16} = s_{\text{TRT}}$. The other three relaxation rates s_1 , s_2 and s_{10} seem to have no effect on the outcome. To evaluate whether s_4 or s_{16} or both are responsible for the small error, either s_4 (MRT-2) or s_{16} (MRT-3) is set to s_{TRT} . Both settings again result in large errors which shows that both relaxation parameters and not only a single one have an effect on the error.

	0.6	1.0	1.5	2.0
SRT	5.06×10^{-3}	1.78×10^{-3}	2.32×10^{-2}	5.88×10^{-2}
TRT	3.06×10^{-8}	1.98×10^{-8}	1.98×10^{-8}	3.36×10^{-8}
MRT	5.10×10^{-3}	4.11×10^{-3}	2.86×10^{-3}	1.62×10^{-3}
MRT-1	3.06×10^{-8}	1.98×10^{-8}	1.98×10^{-8}	3.36×10^{-8}
MRT-2	4.00×10^{-3}	3.96×10^{-3}	3.09×10^{-3}	3.85×10^{-3}
MRT-3	1.33×10^{-3}	1.32×10^{-3}	1.30×10^{-3}	1.28×10^{-3}

Table 3.2: Comparison of the error $E(u)$ of various parameter settings as given in Tab. 3.1 for $\tau = 0.6, 1.0, 1.5, 2.0$.

Conclusion

All in all, the tests indicate that only two relaxation rates, s_4 and s_{16} , influence the error and therefore both should be set to s_{TRT} in order to obtain the correct boundary location and increase the overall accuracy of the simulation. This is not only true for the Poiseuille flow but should be kept in mind for all flow setups where walls play an important role. The other relaxation rates and free parameters, $s_1, s_2, s_{10}, \omega_\epsilon, \omega_{\epsilon j}$ and ω_{xx} , seem to play no role here.

3.2 Lid-driven square cavity flow

The next test case is the well-known lid-driven square cavity flow. With this benchmark test, the stability of different methods can be tested. It consists of a closed square box which is completely filled with fluid being at rest at the beginning of the simulation. The top of the box, the lid, is continually dragged across the fluid, resulting finally in a circular flow of the fluid, called the primary vortex and rotating clockwise. Additionally, smaller vortices will arise at the corners and other locations, which are called the secondary vortices and rotate counter-clockwise, see the sketch in Fig. 3.2. The intensity of these vortices depends on the Reynolds number Re which in this case is defined as

$$Re = \frac{U L}{\nu}, \quad (3.5)$$

where U is the lid velocity, L the length of the lid and ν the kinematic viscosity of the fluid.

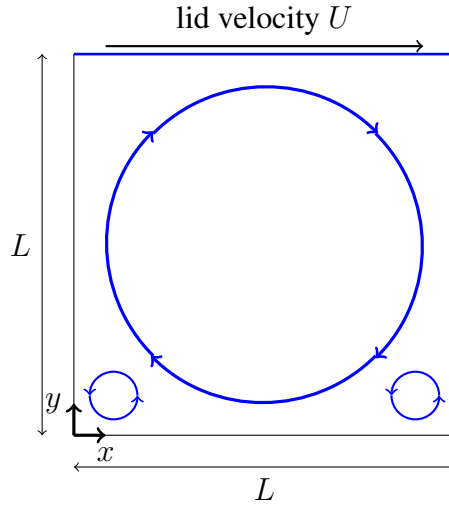


Figure 3.2: Schematic layout of the lid-driven square-cavity.

Setup

The simulation domain is chosen to be $[0, N_x] \times [0, N_y] \times [0, N_z]$, where N_i denotes the number of grid cells in i -direction. All simulations are carried out on a grid with $N_x = N_y = 129$ and $N_z = 3$. Bounce-back boundary conditions are used to model the wall in x - and y -direction. In z -direction, periodic boundary conditions are applied. Simulations with $Re = 100, 1000, 4000$, and 7500 are carried out. Since the lid velocity is held constant throughout all simulation as $U = (0.1, 0, 0)^T$, the Reynolds number is only changed by setting different kinematic viscosities of the fluid. This is done by changing the relaxation time τ , according to Eq. (2.14). The simulation is run for 150000 time steps where it converged for $Re = 100, 1000, 4000$. In the case of $Re = 7500$ no steady state solution can be obtained anymore.

Methods

In this benchmark test, the SRT, TRT and MRT model can be compared regarding their ability to maintain a stable flow and deal with oscillations. It is often stated that one of the main advantages of the MRT model is the increased stability which makes it possible to simulate flows with higher Reynolds numbers. Similar to [9] and [12], the pressure and vorticity contours are investigated at different Reynolds numbers whether they contain oscillations. For the MRT model, the parameters

stated in Eqs. (2.76) and (2.77) are used. But also different parameter settings are chosen to observe which relaxation parameters s_q have effects on the contours and therefore on certain flow properties.

Results

At first, the results for $Re = 100$ are discussed. A plot of the velocity magnitude is shown in Fig. 3.3 where the MRT model was used. As expected, the velocity is highest near the lid and a circulating flow is obtained. The small secondary vortices are clearly visible in the bottom left and right corner. The corresponding plots for the SRT and TRT model look very similar and are therefore not shown.

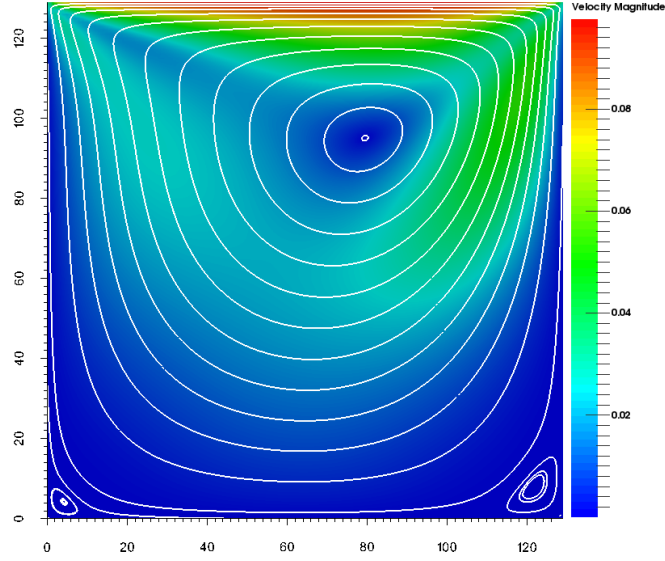


Figure 3.3: Velocity magnitude and streamlines at $Re = 100$ using the MRT model.

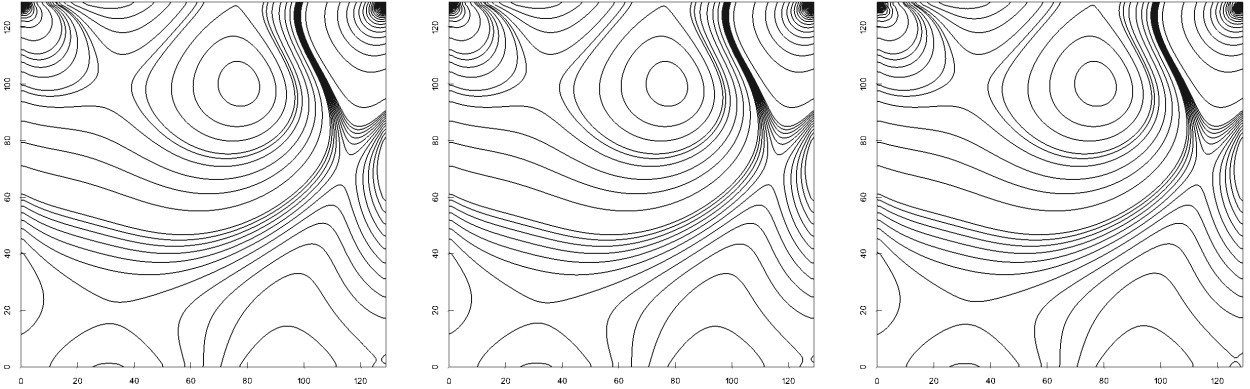


Figure 3.4: Pressure contours at $Re = 100$ using the SRT, TRT and MRT model.

To further compare the results, pressure and vorticity contours of the three models are shown in Figs. 3.4 and 3.5, respectively. Note that the contour lines in the plots are not uniformly distributed over the whole data range because then nearly all lines would be located at the top left and right corners. Instead, for the small data range of the values that are located between the corners, more contour lines are used to capture their shape. Like for the velocity magnitude, they all look the same

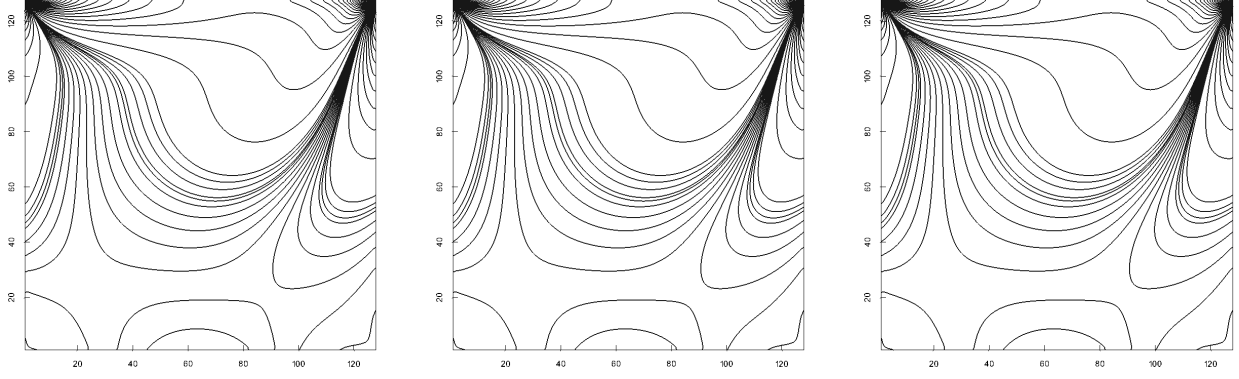


Figure 3.5: Vorticity contours at $Re = 100$ using the SRT, TRT and MRT model.

for the three models. This indicates that at such a low Reynolds number it would not be necessary to use a MRT model since the SRT model is sufficient to capture the important flow features. But since the SRT model introduces again some small inaccuracies near the boundary, one might nevertheless preferably chose the TRT model.

Now the Reynolds number is increased to 1000 and again the different results are compared. As can be seen in Fig. 3.6, the secondary vortices are bigger than in the $Re = 100$ case. But like before, the velocity magnitude plots for the SRT, TRT and MRT models look qualitatively the same.

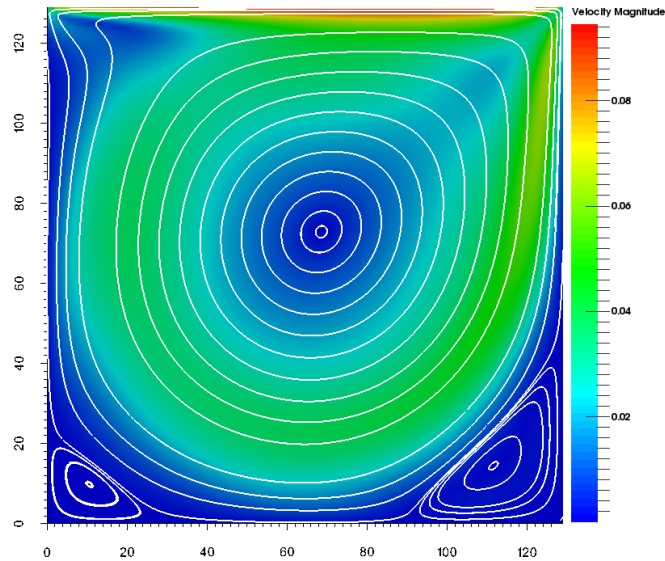


Figure 3.6: Velocity magnitude and streamlines at $Re = 1000$ using the MRT model.

The pressure and vorticity contours plots in Figs. 3.7 and 3.8 illustrate that this time the results of the three models differ significantly from each other. The pressure contours of the SRT model exhibit severe oscillations in the top left corner and some minor ones in the top right corner. In contrast to that, the TRT model yields smooth lines. Unexpectedly, the MRT model also shows some instabilities near the corners which are not as strong as the ones from the SRT model but nevertheless

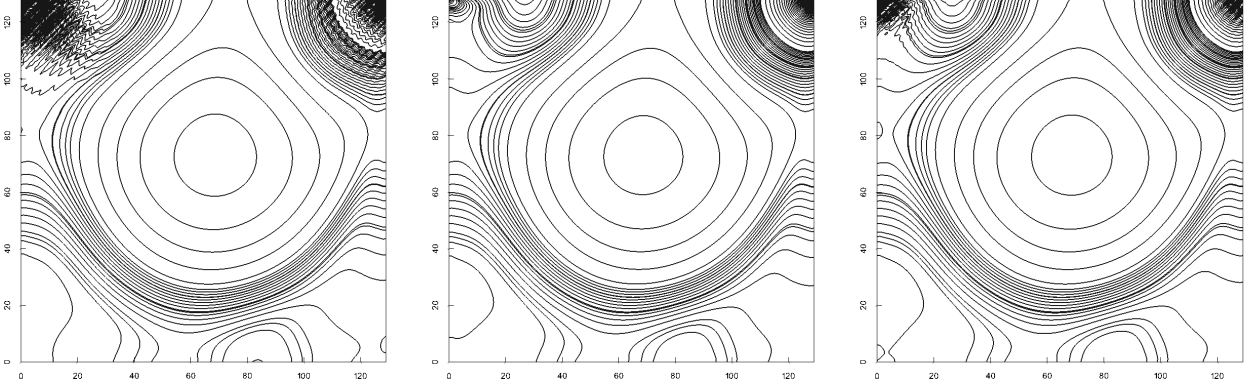


Figure 3.7: Pressure contours at $Re = 1000$ using the SRT, TRT and MRT model.

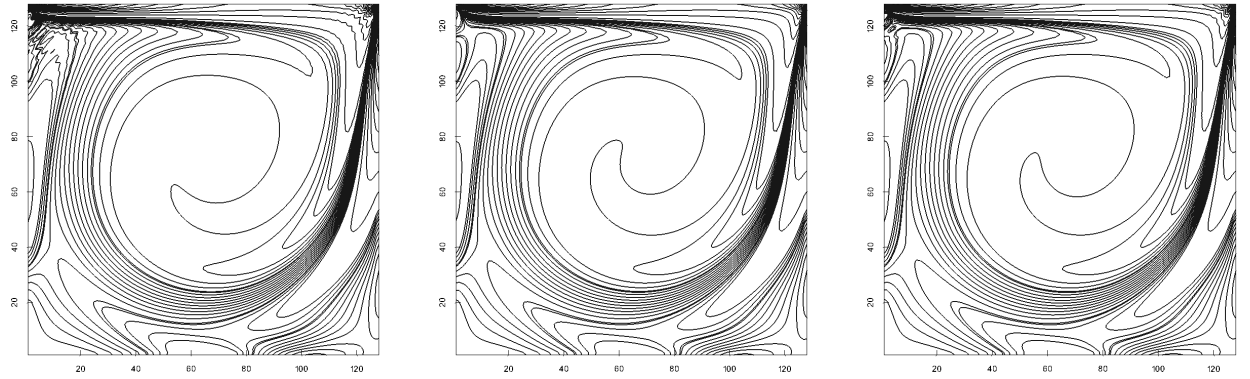
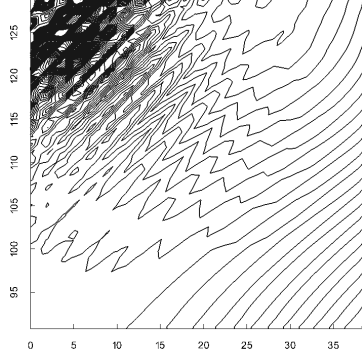


Figure 3.8: Vorticity contours at $Re = 1000$ using the SRT, TRT and MRT model.

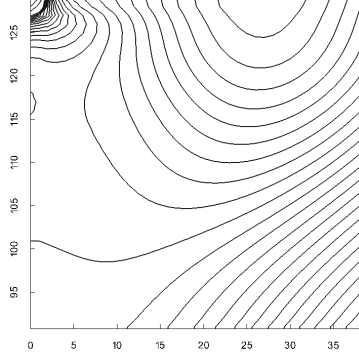
clearly visible. The same behaviour can be observed in the vorticity plots but here the oscillations are overall weaker.

In order to get some hints which relaxation parameters cause these oscillations, several simulations with varying parameter setups are carried out. Since the TRT model produced the best results, the TRT parameter setup is chosen as a basis from which single parameters are changed to analyse the effect on the outcome, cf. Tab. 3.3. The only difference between the SRT and the TRT model are the parameters s_4 and s_{16} but they apparently have a huge effect on the results. Therefore an obvious choice for the parameters is setting either $s_4 = 1/\tau$ (TRT-1) or $s_{16} = 1/\tau$ (TRT-2). Also the effect of changing the equilibrium parameters (TRT-3), s_1 (TRT-4), s_2 and s_{10} (TRT-5) is tested. The last parameter setting uses the original MRT setting but with $s_4 = s_{16} = s_{\text{TRT}}$ (MRT-1), following the findings from the previous section to get a better approximation of the boundary location.

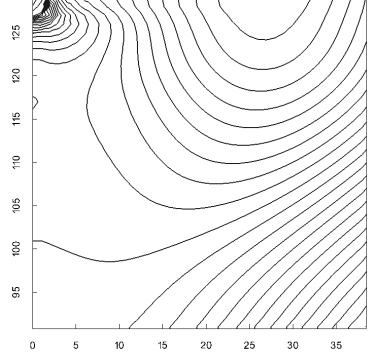
The results of these simulations can be seen in Figs. 3.9 and 3.10 where only the upper left corner is shown since this is the most interesting area of the domain. Comparing the TRT with the TRT-1 case, no significant differences can be seen neither in the pressure contours nor in the vorticity contours. Therefore, one can conclude that s_4 alone has in this case no effect on the pressure and is not the cause of the fluctuations one can see in the SRT case. In TRT-2 on the other hand, small pressure fluctuations can be seen and the vorticity differs slightly from the TRT case. This indicates that the choice of s_{16} influences these properties but is not the only reason for the severe SRT fluctuations. Since the only difference between the SRT and the TRT model are in fact those two relaxation parameters, it seems like the combination of setting both to the rather small value s_{TRT}



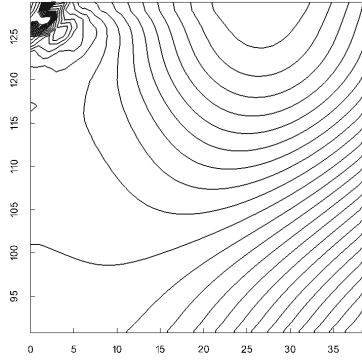
(a) SRT



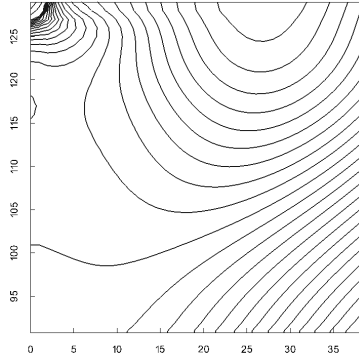
(b) TRT



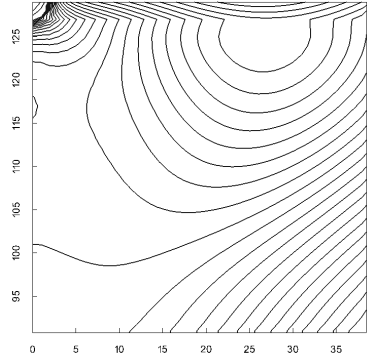
(c) TRT-1



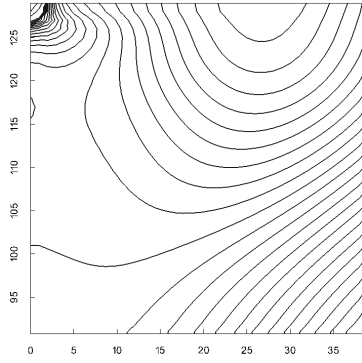
(d) TRT-2



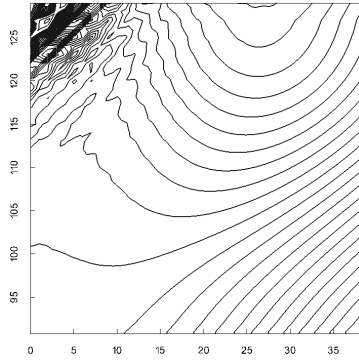
(e) TRT-3



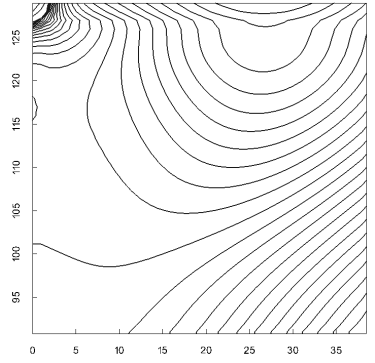
(f) TRT-4



(g) TRT-5

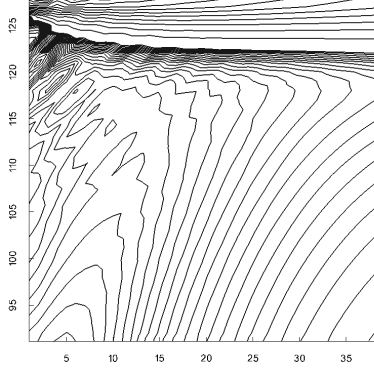


(h) MRT

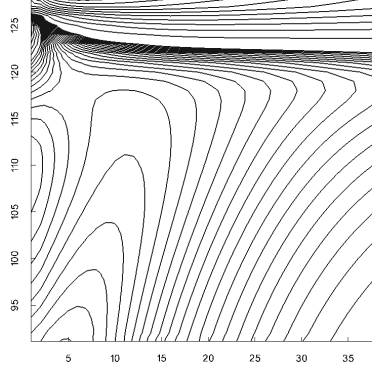


(i) MRT-1

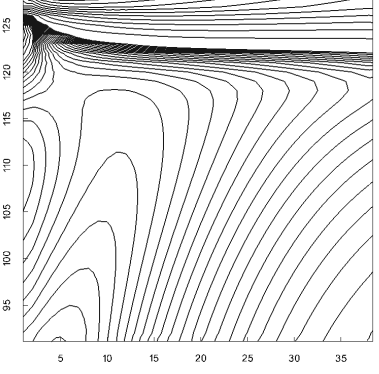
Figure 3.9: Pressure contours at $Re = 1000$ in the upper left corner, $(x, y) \in [0, 38.7] \times [90.3, 129]$, for parameter settings from Tab. 3.3.



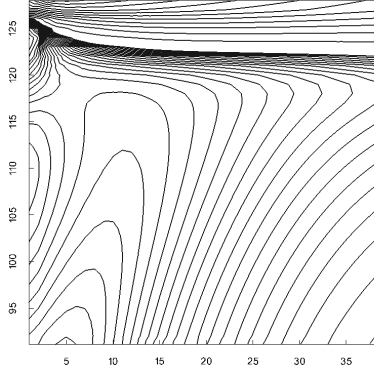
(a) SRT



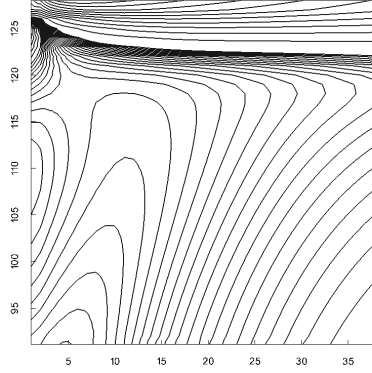
(b) TRT



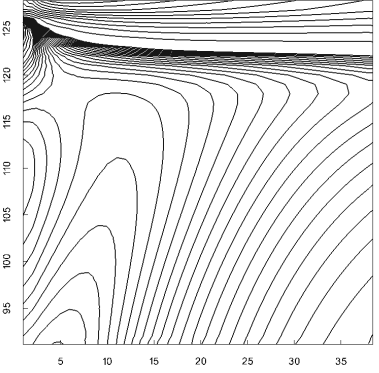
(c) TRT-1



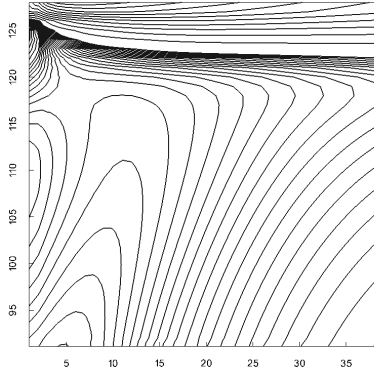
(d) TRT-2



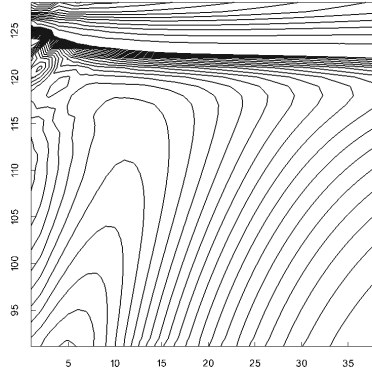
(e) TRT-3



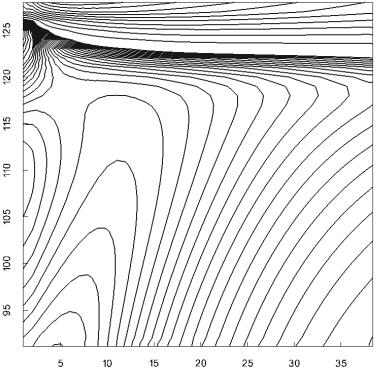
(f) TRT-4



(g) TRT-5



(h) MRT



(i) MRT-1

Figure 3.10: Vorticity contours at $Re = 1000$ in the upper left corner, $(x, y) \in [0, 38.7] \times [90.3, 129]$, for parameter settings from Tab. 3.3.

	s_1	s_2	s_4	s_{10}	s_{16}	ω_s
SRT	$1/\tau$	$1/\tau$	$1/\tau$	$1/\tau$	$1/\tau$	SRT
TRT	$1/\tau$	$1/\tau$	s_{TRT}	$1/\tau$	s_{TRT}	SRT
TRT-1	$1/\tau$	$1/\tau$	$1/\tau$	$1/\tau$	s_{TRT}	SRT
TRT-2	$1/\tau$	$1/\tau$	s_{TRT}	$1/\tau$	$1/\tau$	SRT
TRT-3	$1/\tau$	$1/\tau$	s_{TRT}	$1/\tau$	s_{TRT}	MRT
TRT-4	1.64	$1/\tau$	s_{TRT}	$1/\tau$	s_{TRT}	SRT
TRT-5	$1/\tau$	1.54	s_{TRT}	1.54	s_{TRT}	SRT
MRT	1.19	1.4	1.2	1.4	1.98	MRT
MRT-1	1.19	1.4	s_{TRT}	1.4	s_{TRT}	MRT

Table 3.3: Parameter settings for simulations at $Re = 1000$. $1/\tau \approx 1.856$, $s_{\text{TRT}} \approx 0.1871$, the ω_s are either $\omega_\epsilon = 3, \omega_{\epsilon j} = -11/2, \omega_{xx} = -1/2$ (SRT) or $\omega_\epsilon = 0, \omega_{\epsilon j} = -475/63, \omega_{xx} = 0$ (MRT).

compared to the large value of $1/\tau$ eliminates the fluctuations in both, pressure and vorticity. This is an important point since it follows that it is not possible in general to denote one single parameter that causes some behaviour to happen or not to happen but instead the behaviour can be the result of certain combinations of different parameters. This makes it hard to evaluate general rules for the choice of single parameters. In the actual case here, s_{16} seems to be the source of the fluctuations but the choice of s_4 characterises whether they get eliminated (small values for s_4) or amplified (large value for s_4).

For TRT-3 and TRT-5, no differences to the TRT case can be observed in the pressure or the vorticity. However in the TRT-4 case, a noticeable kink in the pressure appears at the top. Such a kink can not be seen in the vorticity plot which shows no difference to TRT. This indicates that s_1 has a large effect on the pressure at least in the region close to the lid.

When the MRT model is used with the same parameters for s_4 and s_{16} as the TRT model, as shown in the plot of MRT-1, the fluctuations that were clearly visible before vanish. Nevertheless, a similar kink as in the TRT-4 case can be noticed at the top. This again might be the result of choosing $s_1 \neq 1/\tau$.

Therefore, for a Reynolds number of around 1000 it seems best to use the TRT model since one obtains smooth results for pressure, velocity and vorticity with comparable small effort.

Next, the Reynolds number is further increased to 4000. As can be seen in Fig. 3.11, another vortex forms near the top left corner and the centres of the bottom vortices start to move in clockwise direction. This behaviour seems to cause huge problems for the SRT and TRT model because both of them become unstable and diverge. Therefore no results can be shown for them.

Further tests are carried out with the parameter sets from Tab. 3.3. From Tab. 3.4, it can be seen that only the MRT model is able to produce stable and physically meaningful results.

	SRT	TRT	TRT-1	TRT-2	TRT-3	TRT-4	TRT-5	MRT	MRT-1
stable results	×	×	×	×	×	×	×	✓	×

Table 3.4: Stable simulation outcomes for the parameter settings given in Tab. 3.3 at $Re = 4000$.

To further analyse why MRT-1 is now unstable whereas at $Re = 1000$ setting $s_4 = s_{16} = s_{\text{TRT}}$ eliminated the oscillations, two additional parameter settings, MRT-2 and MRT-3 (cf. Tab. 3.5), are simulated. Their pressure and vorticity results are displayed in Figs. 3.12 and 3.13.

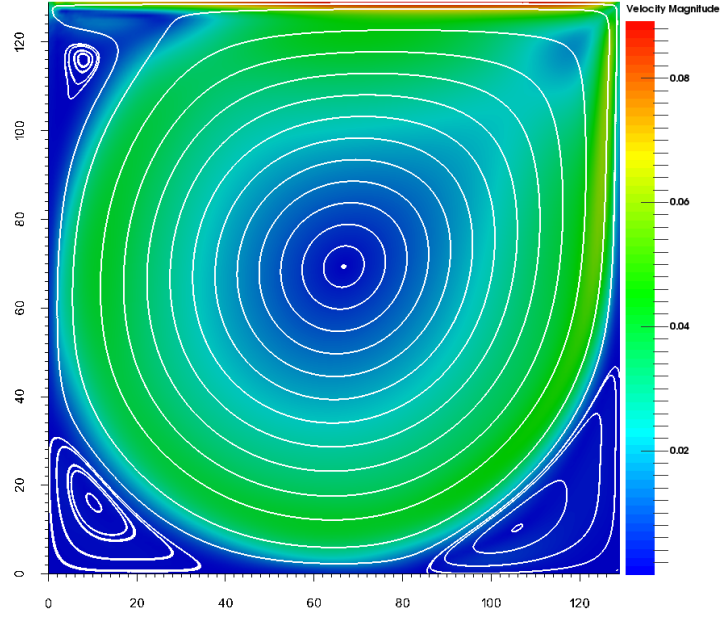


Figure 3.11: Velocity magnitude and streamlines at $Re = 4000$ using the MRT model.

	s_1	s_2	s_4	s_{10}	s_{16}	ω_s	stable results
MRT	1.19	1.4	1.2	1.4	1.98	MRT	✓
MRT-1	1.19	1.4	s_{TRT}	1.4	s_{TRT}	MRT	✗
MRT-2	1.19	1.4	s_{TRT}	1.4	1.98	MRT	✓
MRT-3	1.19	1.4	1.2	1.4	s_{TRT}	MRT	✓

Table 3.5: Parameter settings for further simulations at $Re = 4000$. $s_{\text{TRT}} \approx 0.18709$, ω_s as MRT means $\omega_\epsilon = 0, \omega_{\epsilon j} = -475/63, \omega_{xx} = 0$.

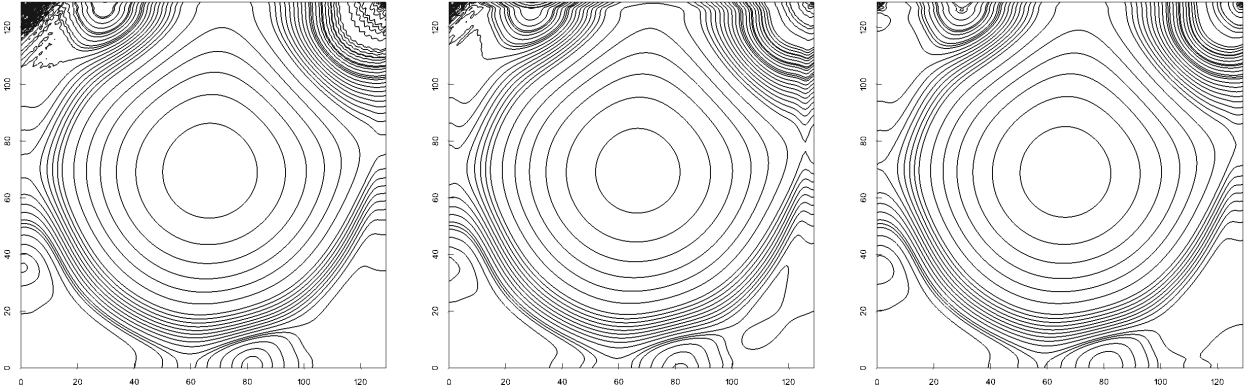


Figure 3.12: Pressure contours at $Re = 4000$ using the MRT, MRT-2 and MRT-3 model from Tab. 3.5.

In the MRT model, very similar oscillations to the $Re = 1000$ case from before can be seen near the top left and right corner of the pressure and the vorticity. But they have not grown further into the domain. When setting $s_4 = s_{\text{TRT}}$ (MRT-2), the oscillations slightly reduce in both plots but a severe

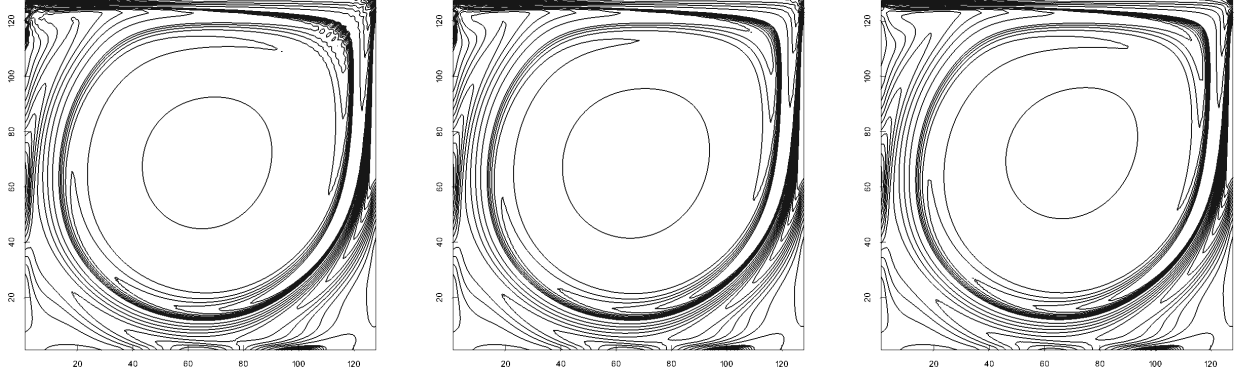


Figure 3.13: Vorticity contours at $Re = 4000$ using the MRT, MRT-2 and MRT-3 model from Tab. 3.5.

kink in the pressure at the top and right wall appears. In the MRT-3 case, the fluctuations in both pressure and vorticity have nearly vanished and no kink is visible. Once again, $s_{16} = s_{\text{TRT}}$ seems to reduce the fluctuations. But in contrast to previous findings, the combination with $s_4 = s_{\text{TRT}}$ does not further improve the results at this Reynolds number but rather causes instabilities.

At last, the Reynolds number is increased to 7500 and it is analysed whether the MRT models are still able to yield some useful information or if the oscillations spread further into the domain, contaminating the results. As expected, all three vortices in the corners grow bigger making the simulation more challenging, cf. Fig. 3.14. But the MRT and the MRT-2 setup still result in useful outcomes whereas MRT-1 and MRT-3 become unstable and fail to converge.

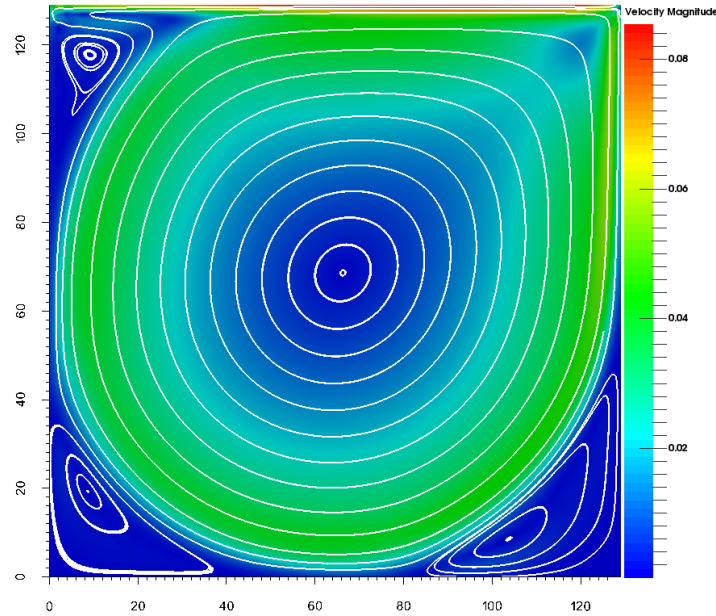


Figure 3.14: Velocity magnitude and streamlines at $Re = 7500$ using the MRT model.

In Fig. 3.15, additionally to the already known oscillations in the top left and right corner,

fluctuations along the right wall are now observable in the pressure contours. Here, MRT-2, which has again a severe kink, has smaller perturbations at the corners but larger ones at the right wall. In the MRT case, vorticity oscillations start to move into the domain, as displayed in Fig. 3.16, whereas MRT-2 shows only some small oscillations directly in the upper corners.

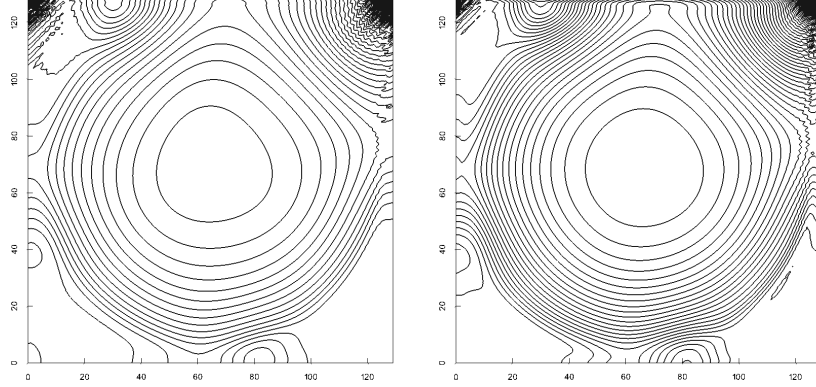


Figure 3.15: Pressure contours at $Re = 7500$ using MRT and MRT-2 from Tab. 3.5.

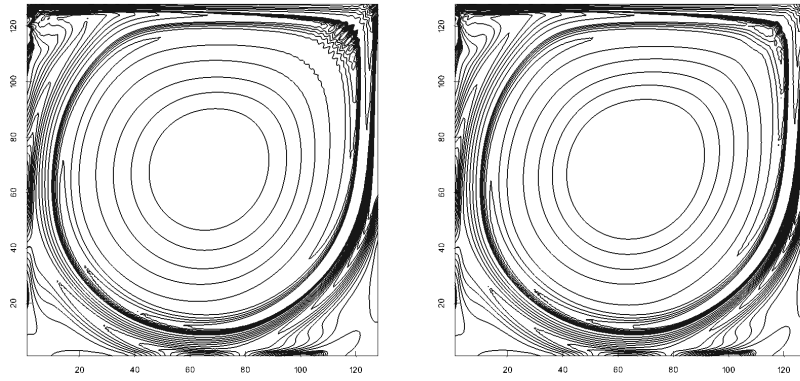


Figure 3.16: Vorticity contours at $Re = 7500$ using MRT and MRT-2 from Tab. 3.5.

Conclusion

For Reynolds numbers up to approximately 1000, the TRT model yields very smooth and good results. But if one wants to simulate higher Reynolds numbers the use of MRT models is inevitable. The simulations suggest that the relaxation parameter s_1 effects the pressure near the boundaries which may lead to severe kinks. s_4 and s_{16} again play a major role here since their choice influences the oscillations near the corners of the domain. With their help, the oscillations can be decreased or even eliminated when setting them to s_{TRT} . Nevertheless, no general rule can be formulated since for higher Reynolds numbers this setting can cause instabilities and divergent solutions. One can also conclude that the MRT setup proposed by d’Humières indeed increases the stability considerably. Even at high Reynolds numbers, both the pressure and the vorticity allow conclusions about the real flow behaviour at least slightly away from the top corners. This makes the MRT models a powerful tool for flow simulations.

3.3 Flow past a square cylinder

After simulations that looked into the accuracy near the wall and the stability, the third test case is carried out to obtain more insight into the correct modelling of physical behaviour. For this purpose, the flow past a square cylinder, also called the Kármán vortex street, is simulated. It is known that behind the cylinder a recirculation area will appear. If the Reynolds number is high enough, vortices will begin to shed and a vortex street will form. The Reynolds number is here defined as:

$$Re = \frac{D U_{max}}{\nu}, \quad (3.6)$$

where D is the side length of the cylinder, U_{max} the maximal inflow fluid velocity (occurring in the vertical channel centre) and ν again the kinematic viscosity.

This vortex shedding has a certain characteristic frequency which is expressed with the help of the dimensionless Strouhal number:

$$St = \frac{f D}{U_{max}}, \quad (3.7)$$

where f is the vortex frequency. This Strouhal number can now be computed and compared with results from the literature (e.g. [13] and [2]) to get information whether the different LBM models are able to get the physical behaviour right and additionally to see the effect of different relaxation parameters on the frequency.

Setup

For this simulation, a channel with resolution $1600 \times 3 \times 240$ is used. A sketch of the geometry can be seen in Fig. 3.17. An important parameter for the flow behaviour is the blocking factor which is calculated as D/H , i.e. the ratio between the side length of the cylinder and the height of the channel. Throughout the simulations, this ratio is set to 12.5%. Therefore, the cylinder has the length $30 \times 3 \times 30$, where the midpoint of the cylinder is placed at around $1/3$ of the channel length and vertically centred.

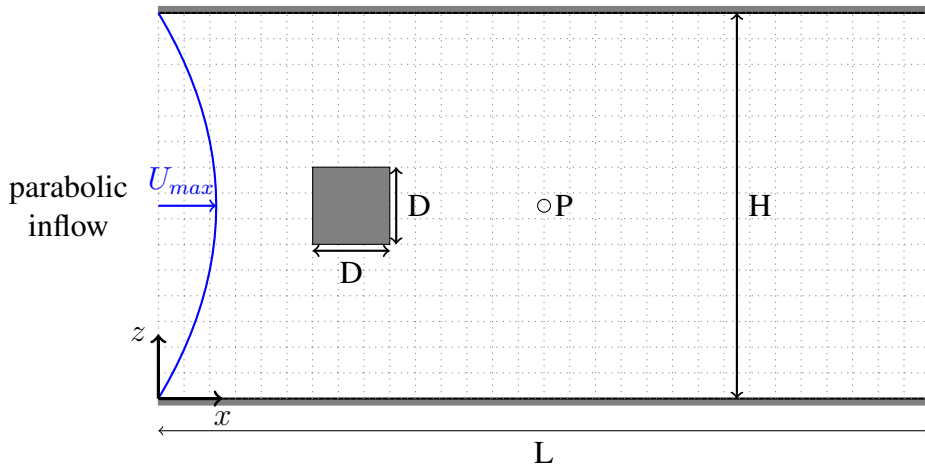


Figure 3.17: Schematic geometry of the channel including the square cylinder.

At the inlet, velocity bounce-back conditions are used. Since the flow has to be fully developed when it encounters the obstacle, the inflow profile is not a uniform but already a parabolic one. The maximal inflow velocity U_{max} is held constant at 0.05. The parabolic velocity profile for a channel

flow can then be calculated using:

$$u_x(z) = 4 \frac{U_{max}}{H^2} z (H - z) \quad (3.8)$$

Streaming in the already developed velocity profile omits the need to make the channel much longer in front of the obstacle to achieve the desired profile, which saves a lot of computing time. At the outlet, pressure anti-bounce-back conditions are used. These prevent that a wave will be reflected at the outlet which would consequently contaminate the simulation domain and the outcome. In y-direction, periodic boundary conditions are used, and in z-direction and on the obstacle itself no-slip conditions are applied.

Methods

The simulations are carried out at two different Reynolds numbers, 80 and 133. Both values appear in [2] and [13], which will serve as a reference. It is known that at $Re = 80$ the separation of vortices starts at the trailing edge of the obstacle, whereas at $Re = 133$ it already tends to start at the leading edge. Plots of the velocity for the first case can be found in Fig. 3.18.

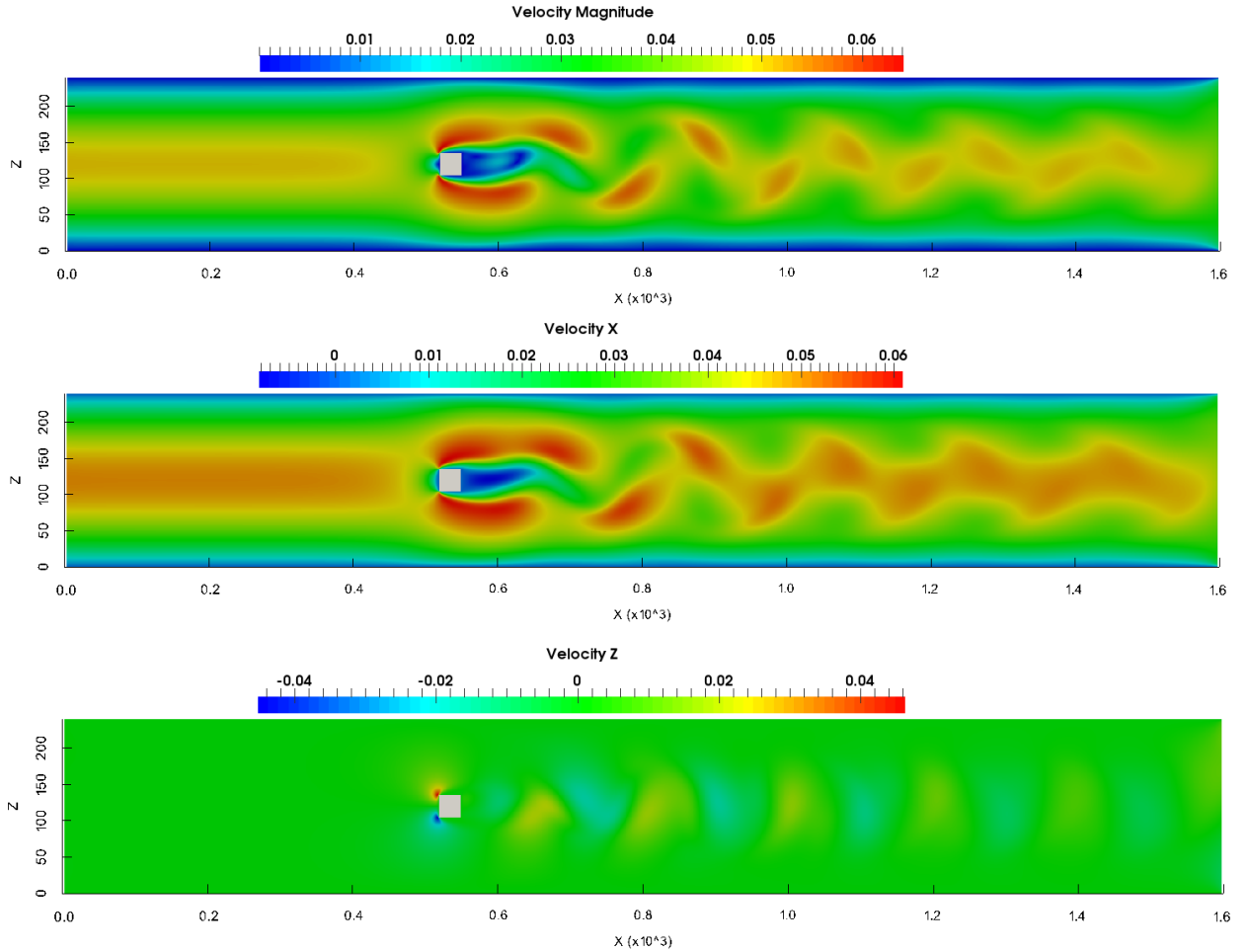


Figure 3.18: Velocity (magnitude, x- and z-component) at $Re = 80$.

The frequency of the resulting vortices can then be evaluated what finally allows to calculate the Strouhal number. For this purpose, the z-component of the velocity field is accessed at the measuring

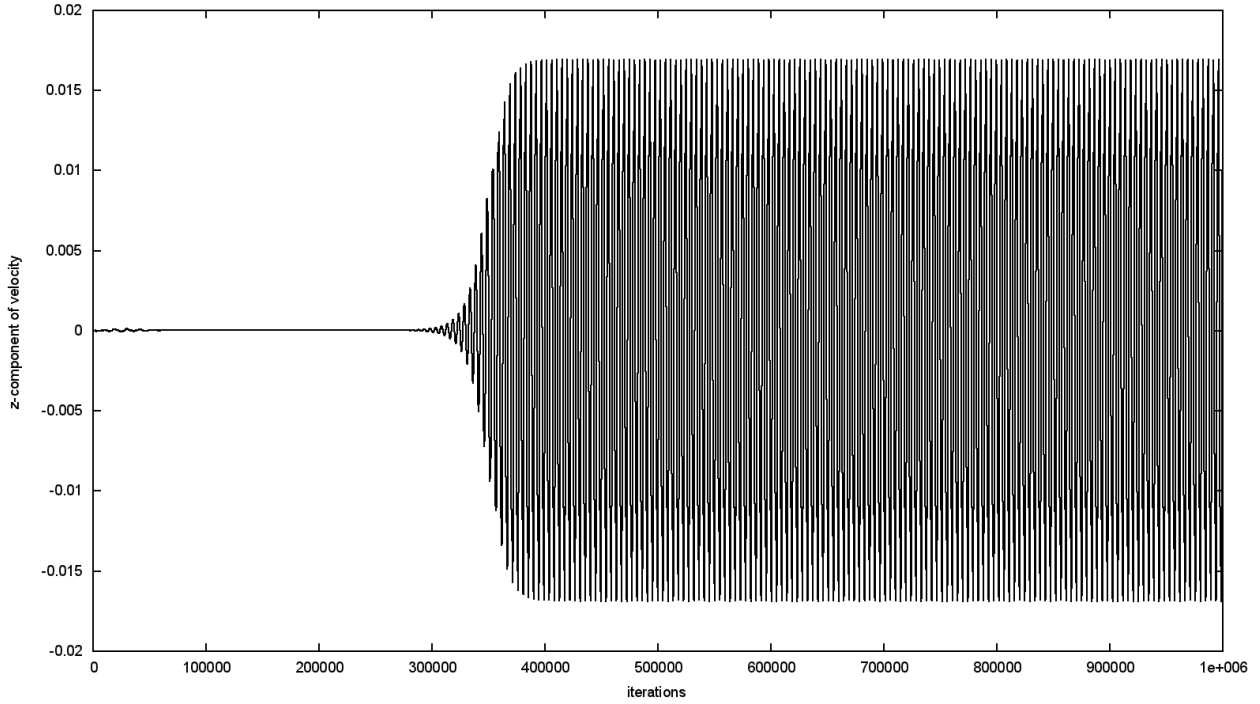


Figure 3.19: Temporal change of the z-component of the velocity at $Re = 80$.

point P which is placed in the centre of the channel with a distance of $10 D$ behind the obstacle, cf. Fig. 3.17. Since it takes a while until the separation begins, the simulation is run 1000000 time steps where the z-component of the velocity is written to a file every 100 time steps. According to [13], this measuring frequency is sufficient to capture the appearing vortex frequencies. A plot of the temporal development of the z-component can be seen in Fig. 3.19, where the start up of the separation until the separation frequency finally becomes constant can be observed.

Out of these measuring results, the last 4096 ones are taken in order to analyse only the constant end frequency. To get the frequency out of them, a discrete fourier transformation (DFT) from the tool xmgrace³ is applied. To increase the resolution of the DFT, 4096 zeros are appended to the original data ([13]). The obtained frequency spectrum is display in Fig. 3.20 as an example where the dominant frequency can clearly by identified. Applying Eq. (3.7), the Strouhal number can then be computed.

Using the SRT, TRT and different MRT models as stated in Tab. 3.6, simulations for the aforementioned Reynolds numbers are carried out and the Strouhal number is computed according to the procedure described before. The deviation from the literature values is evaluated, allowing conclusions about the influence of the different relaxation parameters on the frequency.

Results

In Tab. 3.7, the resulting Strouhal numbers of the simulations can be seen.

For $Re = 80$, the results of the SRT and MRT model are nearly identical and match with the value obtained by Zeiser [13], whereas the Strouhal number for the TRT model is slightly off this value. From the results of MRT-1, MRT-2 and MRT-3 it can be deduced that setting the relaxation parameter s_{16} to a rather small value as it is done in the TRT model might cause this shift in the vortex frequency and therefore also in the Strouhal number.

³<http://plasma-gate.weizmann.ac.il/Grace/>

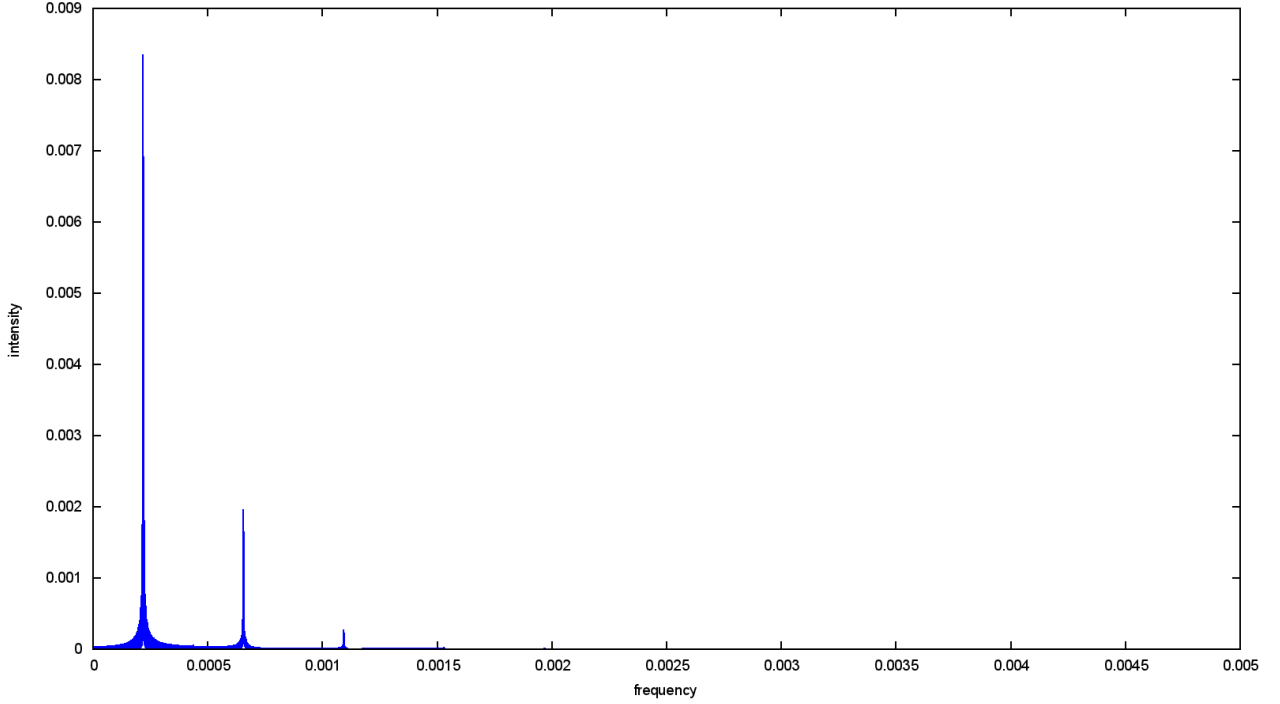


Figure 3.20: Frequency spectrum as obtained after a discrete fourier transformation at $Re = 80$.

	s_1	s_2	s_4	s_{10}	s_{16}
SRT	$1/\tau$	$1/\tau$	$1/\tau$	$1/\tau$	$1/\tau$
TRT	$1/\tau$	$1/\tau$	s_{TRT}	$1/\tau$	s_{TRT}
MRT	1.19	1.4	1.2	1.4	1.98
MRT-1	1.19	1.4	s_{TRT}	1.4	1.98
MRT-2	1.19	1.4	1.2	1.4	s_{TRT}
MRT-3	1.19	1.4	s_{TRT}	1.4	s_{TRT}

Table 3.6: Parameter settings for the Karman vortex street simulations. $Re = 80 : 1/\tau \approx 1.79775$, $s_{\text{TRT}} \approx 0.26087$, $Re = 133 : 1/\tau \approx 1.87324$, $s_{\text{TRT}} \approx 0.165517$.

	SRT	TRT	MRT	MRT-1	MRT-2	MRT-3	Zeiser [13]
$Re = 80$	0.1311	0.1326	0.1311	0.1311	0.1319	0.1319	0.1311
$Re = 133$	0.1465	0.1502	0.1465	0.1472	0.1472	0.1487	0.1442

Table 3.7: Strouhal numbers St of the different models from Tab. 3.6.

For a Reynolds number of 133, a similar outcome can be seen. Again, the SRT and MRT models yield the same Strouhal number which this time differs a bit from the reference value. But results from other simulations done by Breuer et al. [2] suggest that the actual Strouhal number might be a bit higher than the one from Zeiser. The TRT model again leads to a higher Strouhal number as the SRT and MRT models. The MRT-1 outcome indicates that also the choice of s_4 influences the vortex frequency. When setting $s_4 = s_{16} = s_{\text{TRT}}$ as done in MRT-3, both influences on St accumulate and result in an increased Strouhal number compared to the original MRT setting.

Conclusion

The results indicate that mostly s_4 and s_{16} influence the vortex frequency and consequently the Strouhal number. On the one hand, this could be explained by findings from Lallemand and Luo [8]. They derived for the d2q9 model that the relaxation parameter for the heat fluxes, i.e. s_4 , has some influence on the behaviour of waves and it is therefore not desired to have small values for s_4 as it is done when setting it to s_{TRT} . But on the other hand, it got clear from Sec. 3.1 that s_4 and s_{16} influence the placement of the simulated wall. Therefore the simulated obstacle of the TRT model might actually have a different diameter than the obstacle in the SRT or MRT case. And this would consequently alter the vortex frequency.

Overall all three models are capable of predicting the Strouhal number quite accurate and the actual reason for the small differences has to be evaluated further.

4 Summary

In this thesis, the multiple-relaxation-time model for the collision operator in the lattice Boltzmann method has been presented. One of the main ideas there is to carry out the collision not in the velocity space as done in the BGK model but in a newly constructed moment space. This helps to incorporate the physics into the model. For the mapping between these spaces, a transformation matrix is utilised which results in a slightly slower algorithm in comparison to the BGK model. The use of a diagonal collision matrix instead of a single relaxation parameter allows to relax the different moments independently yielding the maximal number of degrees of freedom for the approximation of the linearised collision operator. The d3q19 velocity model features therefore seven relaxation parameters and three additional free parameters. Two of them are linked to the kinematic viscosity and another one is associated with the bulk viscosity. For the other parameters, it has not generally been possible to relate them directly to physical properties. This circumstance has been used as a starting point for three different simulations to investigate further the influence of the parameters on different important properties of the flow. For this purpose, the MRT model has been implemented in the waLBerla framework allowing parallel fluid flow simulations in various domains.

The simulation of a Poiseuille channel flow has aimed at finding out which relaxation parameters are connected to the correct placement of the channel walls. Here, s_4 and s_{16} have been identified and should therefore be given the value obtained by the special formula of the TRT model. To investigate the stability in general and oscillations in the pressure and vorticity, a lid-driven square cavity flow has been set up. The choice of s_4 and s_{16} has again been noted as a core part of the simulations in order to control the appearing fluctuations in the corners. For the parameter s_1 , an influence on the pressure near the walls has been observed. At last, it has been examined whether some parameters influence the Strouhal number defined by the frequency of vortices appearing in the flow behind a square cylinder. Once more, s_4 and s_{16} affected this characteristic number but their effect can be regarded as small.

Putting everything together, it can be noted that for five relaxation parameters, s_1, s_4, s_9, s_{13} and s_{16} , a relation to physical properties or features of the simulation has been found. The choice of the other five remaining parameters, $s_2, s_{10}, \omega_\epsilon, \omega_{\epsilon j}$ and ω_{xx} , had no observable effect on the simulation outcome of the three test cases which makes it hard to give some guidance on how to choose these. Since, however, the parameter setting by d’Humières performed very well, it is generally advised to stick to this choice of the parameters but use the TRT formula for s_4 and s_{16} instead. In certain cases of higher Reynolds numbers, it can be required to give up the correctness of the boundary placement to be able to obtain stable results, i.e. changing also these two later mentioned parameters to the values determined by the stability analysis.

The MRT model offers the maximal flexibility to tune the simulation which allows to set the parameters in such a way that the best possible results can be obtained. To fully make use of this flexibility, it might be necessary to test different parameter settings for a specific simulation setup. But the results presented in this thesis show how one can analyse different flow properties and already give hints on the influence of certain parameters. Additionally, a well-tested start setting for the parameters is provided which should serve as a basis for further simulations.

References

- [1] P. L. Bhatnagar, E. P. Gross, and M. Krook. A model for collision processes in gases. i. small amplitude processes in charged and neutral one-component systems. *Physical review*, 94(3):511, 1954.
- [2] M. Breuer, J. Bernsdorf, T. Zeiser, and F. Durst. Accurate computations of the laminar flow past a square cylinder based on two different methods: lattice-boltzmann and finite-volume. *International Journal of Heat and Fluid Flow*, 21(2):186–196, 2000.
- [3] D. d’Humières. Generalized lattice-boltzmann equations. *Rarefied gas dynamics- Theory and simulations*, pages 450–458, 1992.
- [4] D. d’Humières. Multiple-relaxation-time lattice boltzmann models in three dimensions. *Philosophical Transactions of the Royal Society of London. Series A:Mathematical, Physical and Engineering Sciences*, 360(1792):437–451, 2002.
- [5] I. Ginzburg and D. d’Humières. Multireflection boundary conditions for lattice boltzmann models. *Phys. Rev. E*, 68:066614, 2003.
- [6] I. Ginzburg, F. Verhaeghe, and D. d’Humières. Two-relaxation-time lattice boltzmann scheme: About parametrization, velocity, pressure and mixed boundary conditions. *Communications in computational physics*, 3(2):427–478, 2008.
- [7] F. J. Higuera, S. Succi, and R. Benzi. Lattice gas dynamics with enhanced collisions. *EPL (Europhysics Letters)*, 9(4):345, 1989.
- [8] P. Lallemand and L.-S. Luo. Theory of the lattice boltzmann method: Dispersion, dissipation, isotropy, galilean invariance, and stability. *Phys. Rev. E*, 61:6546–6562, 2000.
- [9] L.-S. Luo, W. Liao, X. Chen, Y. Peng, and W. Zhang. Numerics of the lattice boltzmann method: Effects of collision models on the lattice boltzmann simulations. *Phys. Rev. E*, 83:056710, 2011.
- [10] C. Pan, L.-S. Luo, and C.T. Miller. An evaluation of lattice boltzmann equation methods for simulating flow through porous media. 2004.
- [11] D. A. Wolf-Gladrow. *Lattice-gas cellular automata and lattice Boltzmann models: an introduction*. Number 1725. Springer, 2000.
- [12] J.-S. Wu and Y.-L. Shao. Simulation of lid-driven cavity flows by parallel lattice boltzmann method using multi-relaxation-time scheme. *International journal for numerical methods in fluids*, 46(9):921–937, 2004.
- [13] T. Zeiser. Numerische Simulation der instationären Umströmung eines quadratischen Zylinders mit dem Lattice Boltzmann Verfahren. LSTM-Erlangen, 1998.